Research paper

Discovery of 1-benzhydryl piperazine-based HDAC inhibitors with anti-cancer and anti-metastatic properties against human breast cancer: synthesis, molecular modeling, *in vitro* and *in vivo* biological evaluation

Dusan Ruzic[a*], Milos Petkovic[b], Nemanja Djokovic[a], Juan F. Santibanez[c,d], Bernhard Ellinger[e,f], Milan Beljkas[a], Sheraz Gul[e,f], Ana Djuric[g], A. Ganesan[h], Aleksandar Pavic[i], Tatjana Srdic-Rajic[g] and Katarina Nikolic[a*]

[a] Department of Pharmaceutical Chemistry, Faculty of Pharmacy, University of Belgrade, Vojvode Stepe 450, 11221 Belgrade, Serbia
[b] Department of Organic Chemistry, Faculty of Pharmacy, University of Belgrade, Vojvode Stepe 450, 11221 Belgrade, Serbia
[c] Group for Molecular Oncology, Institute for Medical Research, University of Belgrade, Dr. Subotića 4, 11129 Belgrade, Serbia
[d] Centro Integrativo de Biología y Química Aplicada, Universidad Bernardo O'Higgins, Chile 8370993, Chile
[e] Fraunhofer Institute for Translational Medicine and Pharmacology ITMP, Hamburg, Germany
[f] Fraunhofer Cluster of Excellence for Immune-Mediated Diseases (CIMD), Hamburg, Germany
[g] Department of Experimental Oncology, Institute for Oncology and Radiology of Serbia, Pasterova 14, 11000, Belgrade, Serbia
[h] School of Pharmacy, University of East Anglia, Norwich Research Park, NR4 7TJ Norwich, United Kingdom
[i] Institute of Molecular Genetics and Genetic Engineering, University of Belgrade, Vojvode Stepe 444a, 11000 Belgrade, Serbia

* Corresponding authors.
E-mail addresses: dusan.ruzic@pharmacy.bg.ac.rs (D. Ruzic),
katarina.nikolic@pharmacy.bg.ac.rs (K. Nikolic).

Highlights

- *In silico* fragment search identified 1-benzhydryl piperazine for synthesis of selective HDAC6 inhibitors.
- Changes in the nature of hydrocarbon linker yielded two nanomolar HDAC6 inhibitors, **6b** and **9b.**
- **8b**, as a non-selective HDAC inhibitor, and **9b** have been evaluated and compared using *in vitro* and *in vivo* assays.
- **8b** showed promising anti-cancer and anti-metastatic effects *in vitro* and *in vivo.*

Abstract

Isoform-selective histone deacetylase (HDAC) inhibition is promoted as a rational strategy to develop safer anti-cancer drugs compared to non-selective HDAC inhibitors. Despite this presumed benefit, considerably more non-selective HDAC inhibitors have undergone clinical trials. In this report, we detail the design and discovery of potent HDAC inhibitors with 1-benzhydryl piperazine as a surface recognition group that differ in hydrocarbon linker. Surprisingly, *in vitro* HDAC screening identified two selective HDAC6 inhibitors (**6b**, IC_{50} = 186 nM and **9b**, IC_{50} = 31 nM), as well as two non-selective nanomolar HDAC inhibitors (**7b** and **8b**). The influence of linker chemistry of synthesized inhibitors on HDAC6 potency was studied using structure-based molecular modelling. The breast cancer cell-lines (MDA-MB-231 and MCF-7) were used to evaluate compound mediated *in vitro* anti-cancer, anti-migratory, and anti-invasive activities, leading to **8b** as the most promising compound. In our study, **8b** is identified as the HDAC inhibitor with very potent anti-angiogenic, anti-metastatic and anti-tumor effects in zebrafish MDA-MB-231 xenograft models at low micromolar concentrations.

1. Introduction

Triple-negative breast cancer (TNBC) presents an aggressive subtype of breast cancer with inferior survival outcomes, as it lacks molecular biomarkers such as estrogen receptor (ER), progesterone receptor (PR), and human epidermal growth factor receptor 2 (HER2)[1]. Globally, it is estimated that TNBC accounts for 15–20% of patients with breast cancer diagnosis[2]. At the time of diagnosis, the frequency of distant metastasis is found in approximately 40% of patients with TNBC. Availability of endocrine therapy and HER2-targeted drugs is associated with better survival in ER-positive and HER2 receptor-positive diseases, whereas cytotoxic chemotherapy remains as a predominant treatment option for patients with early-stage and advanced-stage TNBC[3,4]. Owing to its high incidence of metastases, development of small molecules for such therapeutically elusive disease remains a remarkably challenging field.

In the era of precision oncology, epigenetic alterations are recognized as significant molecular hallmarks that contribute to breast tumorigenesis. Despite the role of epigenetics in cancer initiation events, the activation of invasion and metastasis are connected with epigenetic abnormalities[5,6]. An imbalance in post-translational modifications of histones, such as histone lysine acetylation and deacetylation is closely linked to tumor initiation and progression[7]. The reversible nature of histone post-translational acetylation is mediated by two families of enzymes, histone acetyltransferases (HATs) and histone deacetylases (HDACs). HDACs can be involved either in cancer initiation events (induction of apoptosis[8], differentiation[9], cell-cycle arrest[10] and mitochondrial stress[11]) or in cancer progression events (migration[12], invasion[13] and angiogenesis[14]).

In the human proteome, there are 11 known HDACs (named HDAC1-11) that are zinc-containing metalloenzymes and 7 NAD^+-dependent histone deacetylases (known as sirtuins 1 -7)[15]. The first resolution of crystal structure of a histone deacetylase-like protein in complex with its inhibitors [16] provided three key components of the general pharmacophore required for HDAC inhibition, namely a surface recognition group (CAP group), hydrocarbon linker (aliphatic or aromatic linker) and the zinc-binding group (ZBG) which acts as a warhead (Figure 1A)[16]. Thus far, many HDAC inhibitors (HDACi) have been designed and synthesized[17], with five of them currently used in chemotherapy of hematological malignancies (Figure 1B). Hydroxamic acid is the most widely used ZBG, which is present in the marketed drugs such as vorinostat, belinostat and panobinostat. Others include the natural product romidepsin which has an alternative ZBG as it is a prodrug that possesses a disulfide bond, which upon metabolism releases a zinc-binding thiol group and the 2-aminobenzamide inhibitor, tucidinostat (Figure 1B).
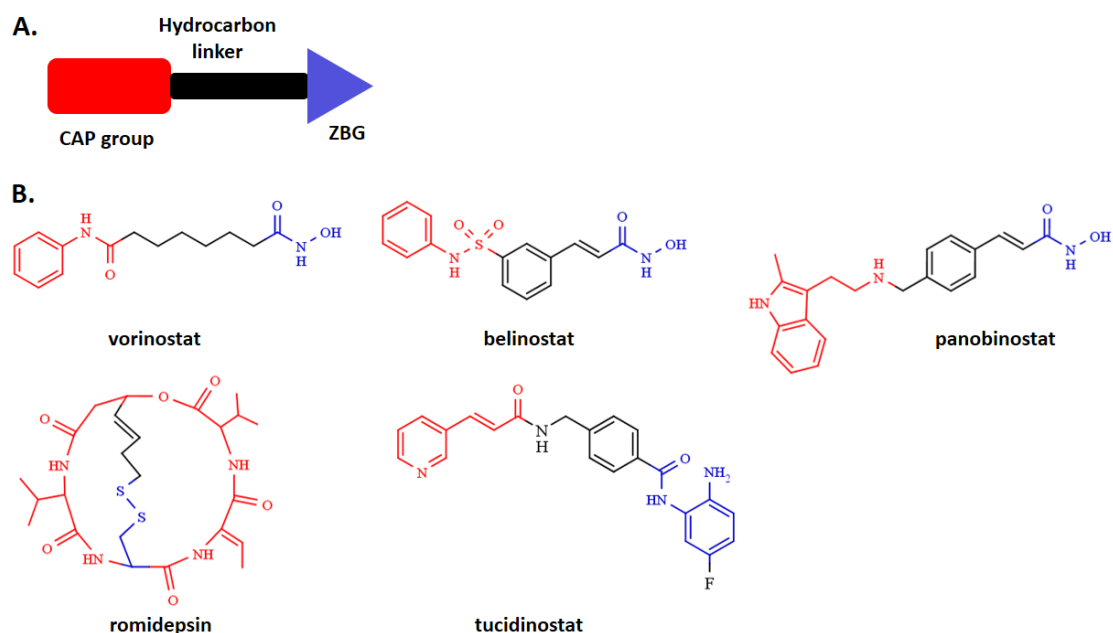
Figure 1. The general pharmacophore model for HDAC inhibitors (A) and chemical structures of five FDA-approved HDAC inhibitors (B).

For more than a decade, HDAC6 has been studied as a promising target for cancer metastasis amongst the human histone deacetylases (HDACs)[18–21]. Unlike most of the human HDACs, the HDAC6 isoform is localized primarily in the cytosol and hydrolyzes terminal N-acetyl-lysine residues of a wide spectrum of the non-histone proteins (e.g. α-tubulin, cortactin and heat-shock protein 90)[22,23]. A unique feature of HDAC6 is the presence of two-catalytic domains (CD1 and CD2) that show diverse substrate specificity and kinetics[24,25], a feature that contrasts markedly with the class I HDACs (e.g. HDAC1, HDAC2, HDAC3 and HDAC8 isoforms). The outer rim of the HDAC6 isoform is significantly wider than in class I HDACs, which is one of the prerequisites for inhibitors to target HDAC6 isoform with higher affinity[26]. Its cellular localization and non-epigenetic roles in cancer progression provide a rationale for therapeutic use of selective HDAC6 inhibitors in pre-clinical metastasis models[27–29]. However, selective HDAC6 inhibitors alone were reported to be inadequate as anti-cancer compounds and it was suggested that an anti-metastatic drug should be a non-selective HDACi or a selective HDAC6i in combination with other chemotherapeutics[30]. It is noteworthy that the FDA-approved HDACi (Figure 1B) are pan-active hydroxamic acid derivatives (vorinostat, belinostat and panobinostat) which show anti-metastatic effects in breast cancer through epigenetic mechanisms of gene expression (inhibition of class I HDACs)[31].

The question whether selective HDAC6 or pan-HDAC inhibitors have better anti-metastatic effects is still disputed. A thorough search of the relevant literature revealed that nine isozymes out of eleven metal-dependent HDACs have been linked to the metastatic events in breast cancer (Supplementary Table S1). As there are many ambiguous reports on antimetastatic HDACi, we were encouraged to design anti-metastatic HDAC inhibitors by use of a single capping group (1-benzhydryl-piperazine), hydroxamic acid as ZBG and diverse hydrocarbon linkers. Here, we report synthesis and *in vitro* and *in vivo* biological profiling of novel HDAC inhibitors bearing 1-benzhydryl piperazine scaffold. This culminated in the identification of selective HDAC6 inhibitor **9b** and a pan-HDAC inhibitor **8b**, both displaying nanomolar potencies against HDAC6 isoform.

2. Results and discussion

2.1. Design and synthesis of HDAC inhibitors

2b – 9b were synthesized using the routes represented in **Figure 2**. The main idea in designing novel HDACi was to employ the 1-benzhydryl piperazine as a CAP group. Computational fragment-based screening reported in our previous study identified many interesting CAP groups for the design of HDAC6 inhibitors[32]. We used 1-benzhydryl piperazine as a template to calculate the total Surface Area (SA$_{tot}$) and McGowan Volume (V$_x$) in the Dragon v. 6.0.7. Software[33] and compared these values with the same descriptors calculated for the CAP groups of ACY-1083[34], tubastatin A[35] and Ricolinostat[36]. These inhibitors exhibited HDAC6 selective inhibitory profiles and diversity in the chemistry of CAP groups. Comparing to SA$_{tot}$ and V$_x$ descriptors, we showed that 1-benzhydryl piperazine exerted higher values for the total Surface Area and McGowan Volume (**Figure 2**) that are important for the inhibitor's complementarity with the HDAC6 interacting surface area.

The alkylation of 1-benzhydryl piperazine with bromo-alkyl methyl esters (n =1–7) in refluxing acetonitrile produced the 1-benzhydryl piperazine methyl ester derivatives (Exp. Procedure 4.2) with aliphatic chains (**2a−8a**) and benzyl-methyl ester derivative (**9a**) at room temperature. Finally, methyl esters (**2a−9a**) were treated with freshly prepared solutions of hydroxylamine in methanol, yielding eight hydroxamic acid derivatives (**2b – 9b, Figure 2,** Exp. Procedure 4.3).
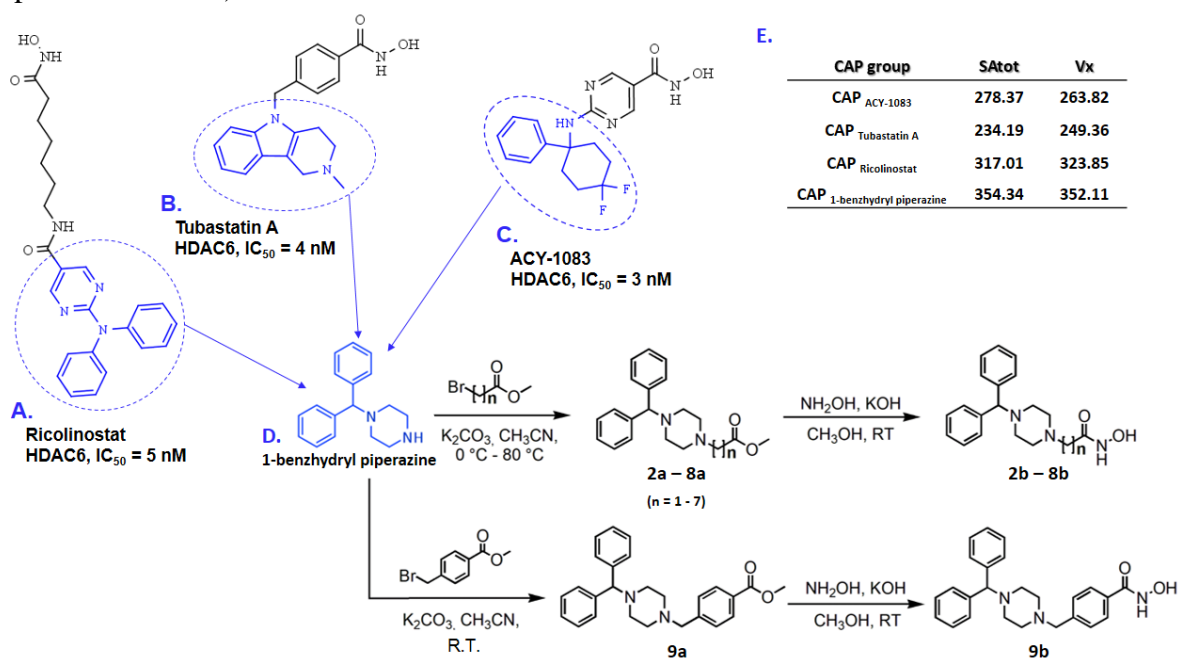

Figure 2. Examples of selective HDAC6 inhibitors: (**A**) Ricolinostat, (**B**) tubastatin A and (**C**) ACY-1083 which CAP groups are labeled in blue; **D**. synthetic routes to produce final products **2b – 9b** starting from 1-benzhydryl piperazine (CAP group) are presented on the bottom right corner; n represents the number of carbon atoms in the hydrocarbon linker; (**E**) Table with calculated SA$_{tot}$ and V$_x$ descriptors for selected CAP groups and 1-benzhydryl piperazine as a template are presented in the right upper corner.

2.2. Biology

2.2.1. Analysis of HDAC inhibitory profiles

The designed and synthesized **2b** to **9b** were screened using a commercial *in vitro* biochemical luminescence assay kit with purified HDAC enzymes. This assay technology has been adequately validated using reference HDACi with a wide potency range (valproic acid, sodium butyrate and Trichostatin A) and a variety of HDAC enzymes[37].

To identify selective HDAC6 inhibitors, a preliminary screening at 5 µM concentration of the synthesized compounds was performed to determine the percentage of HDAC6 inhibition. As it is presented in **Table 1**, compounds with 1, 2, 3, and 4 carbon atoms in the aliphatic linker (**2b**, **3b**, **4b** and **5b**) inhibited HDAC6 isoform in less than 25% at 5 µM.

Table 1. HDAC6 inhibition data for **2b** to **9b**.

	% HDAC6 inhibition at 5 µM							
Compound	2b	3b	4b	5b	6b	7b	8b	9b
	12.2±1.7	22.2±1.1	3.1±1.7	18.2±1.7	95.6±0.9	97.1±0.8	97.7±0.2	96.9±0.3

Percentage inhibitions are expressed as means ± standard errors of triplicate measurements.

When considering that the HDAC6 isoform was sensitive to **6b**, **7b**, **8b** and **9b** (percent inhibition >90% at 5 µM), we conducted HDAC selectivity studies to determine their IC_{50} values against the HDAC1, HDAC3, HDAC6 and HDAC8 isoforms. Nanomolar inhibitory activities toward the HDAC6 isoform were observed for the 1-benzhydryl derivatives with linker lengths of n = 5, 6 and 7, whereas the phenylhydroxamic derivative (**9b**) showed the most potent HDAC6 inhibition (IC_{50} = 31 nM). It can also be concluded from the HDAC selectivity study, that all assayed compounds yielded noticeable HDAC6 selectivity (Figure S1 A-D, Supp. Info), with **9b** displaying the highest selectivity ratio over the HDAC1 (47.5), HDAC3 (112) and HDAC8 (23) isoforms. This observation is in agreement with HDAC6 selectivity inhibition observed for other phenyl-hydroxamic derivatives[38]. Within the group of alkyl-hydroxamic acid derivatives, it appears that optimal linker length should be n = 5 to retain nanomolar and selective HDAC6 potency (**6b**, IC_{50} = 186 nM), which contrasts with the micromolar IC_{50} values toward nuclear isoforms HDAC1/3/8. An increase in the linker length (n = 6 for **7b** and 7 for **8b**) led to a decrease in the selectivity ratios compared to the compound **6b**.

Table 2. Enzymatic *in vitro* profiles of novel hydroxamic acid 1-benzhydryl-piperazine derivatives against HDAC1, HDAC3, HDAC6 and HDAC8 isoenzymes.

Compound	HDAC inhibition, IC_{50} ± SD (µM)				Selectivity ratio		
	HDAC1	HDAC3	HDAC6	HDAC8	HDAC1/6	HDAC3/6	HDAC8/6
6b	4.730 ± 0.670	1.860 ± 0.090	0.186 ± 0.005	2.440 ± 0.510	25.4	10	13.1
7b	0.619 ± 0.023	0.267 ± 0.019	0.096 ± 0.008	0.345 ± 0.017	6.4	2.8	3.6
8b	0.408 ± 0.022	0.207 ± 0.014	0.124 ± 0.013	0.245 ± 0.002	3.3	1.7	2
9b	1.474 ± 0.172	3.467 ± 0.121	0.031 ± 0.004	0.708 ± 0.045	47.5	111.8	23

Valproic acid[#]	660	>1000	>1000	103	-	-	-
Sodium butyrate[#]	8,3	4,8	>1000	10,4	-	-	-
Trichostatin A[#]	0.0013	0.0015	0.0036	0.400	0.3	0.4	111.1

Values are expressed as the mean ± SD of three independent experiments. [#] Profiles of reference HDACi[37].

To further rationalize effects of different linkers on the potency and selectivity profiles of the HDACi, structure-based molecular modeling study of interactions between HDAC6 and synthesized inhibitors was performed. **6b**, **7b**, **8b** and **9b** were initially docked into the crystal structure of the second catalytic domain of human HDAC6 isoform (PBD: 5EDU), and the dynamics of the interaction of selected inhibitors with HDAC6 was investigated by the means of molecular dynamics (MD) simulations (Supp. Info).

Root-Mean-Square-Deviation (RMSD) analysis of HDAC6 backbone atoms movements during 100 ns of MD simulations, indicated well-converged systems without any larger conformational changes of HDAC6 (Figure S2, Supp. Info). Visual inspections of trajectories obtained after MD simulations with RMSD analysis of the ligand atoms, revealed a relationship between the nature of the linker and conformational flexibility of ligands when interacting with HDAC6. Namely, the presence of an aromatic linker conferred a significant increase in conformational stability of the **9b** interaction with HDAC6, compared to the ligands with aliphatic linkers (Figure S2B, Supp. Info). This noticeable difference in dynamic behavior of ligands with aliphatic and aromatic linkers could be the reason for the highest HDAC6 inhibitory potency observed for **9b**, which is in agreement with the study of Porter et al.[39]

The predicted binding modes of all studied inhibitors were in alignment with available X-ray crystal structures where linker is sandwiched between F620 and F680 of aromatic crevice of HDAC6, and CAP groups interact with L1 and/or L2 pockets at the mouth of HDAC6 active site (Figure 3, Figures S3-S6, Supp. Info)[40]. The results of the MD simulations revealed that increasing the length of aliphatic linkers from 5 to 7 C-atoms contributed to considerable differences in binding modes of **6b**, **7b** and **8b**. In contrast, **6b** retained a similar binding mode as ligand **9b** preferably interacting with L2 pocket (Figure 3A), and **7b** interacted rather with L1 pocket (Figure 3B). Due to the presence of the longest linker in **8b**, binding mode of this inhibitor was able to shift between L1 and L2 pockets, which is reflected as a bimodal distribution of distances between centers of masses of the CAP group and L1 or L2 pockets (Figure 3C and Figure S6). This observation is in agreement with binding conformations observed in X-ray crystal structure of HDAC6-ricolinostat complex[39].
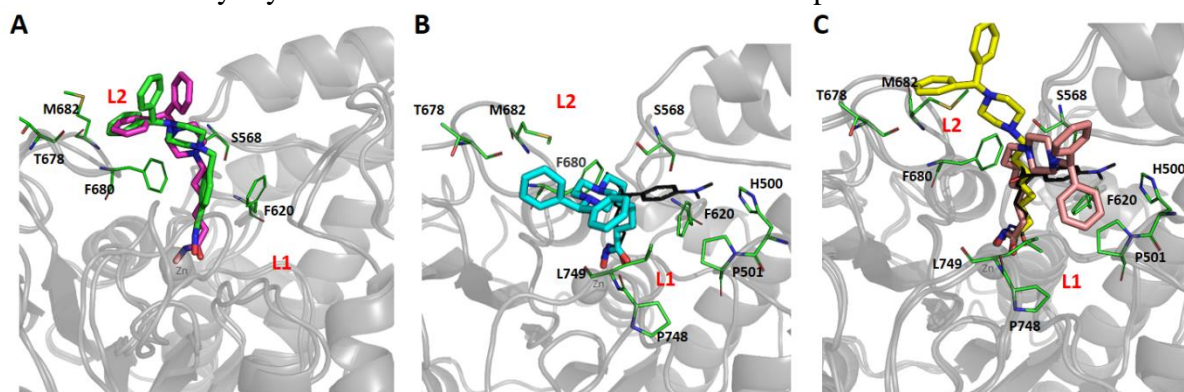

Figure 3. Predicted binding modes of superimposed **6b** (green sticks, **A**) and **9b** (magenta sticks, **A**), **7b** (cyan sticks, **B**) and **8b** (yellow and salmon sticks, **C**) in complex with CD2

HDAC6. Interacting amino acid residues from L1 and L2 pockets are represented in green sticks; co-crystal TSA ligand is presented in black lines.

Based on the results of our studies, **6b** and **9b** represent the most selective HDAC6 inhibitors, which also have similar predicted binding modes (Figure 3A) implying that linker length of 5 C-atoms (n = 5) is optimal for achieving selective interaction with HDAC6 in the series of inhibitors with aliphatic linkers. Taken together, the *in silico* results provided the atomic resolution of the interactions of novel inhibitors with the HDAC6 isoform. Additionally, considering that our selective HDAC6 inhibitors (**6b** and **9b**) uniquely anchor 1-benzhydryl piperazine moiety in L2 pocket, substituting phenyl rings in 1-benzhydryl piperazine appears to be a strategy to target protein landscape in L2 loop pocket and designing novel selective HDAC6 inhibitors.

2.2.2. **Examination of cytotoxic effects of synthesized compounds**

The ability of the designed and synthesized HDACis (**6b**, **7b, 8b** and **9b**) to decrease the viability of studied breast cancer cell lines (MDA-MB-231 and MCF-7) was subsequently investigated. Treatment of breast cancer cells with the HDACis for 48 h resulted in a moderate dose-dependent cytotoxicity as summarized in Table 3 and Figure S8 (Supp. Info). All tested compounds reduced the viability of MDA-MB-231 breast cancer cells at lower concentrations, compared to MCF-7 cells. The obtained IC_{50} values were 33.40 μM, 10.55 μM, 5.42 μM and 38.1 μM for **6b, 7b, 8b and 9b,** respectively. Compound **8b** significantly decrease the viability of MCF-7 cells (IC_{50} = 39.10 μM), whereas the selective HDAC inhibitors **6b** and **9b** reduced cell viability at higher concentrations (IC_{50} were 84.05 μM and 99.50 μM, respectively). The inhibitor **7b** did not exhibit cytotoxic effects against MCF-7 cells (IC_{50} >100 μM). Both selective HDAC6 inhibitors **6b** and **9b** show moderate cancer cell cytotoxicity in the tested breast cancer cell lines, which is consistent with previous studies in breast cancer cell lines[41]. In order to understand the mechanisms of breast cancer cell death upon exposure to tested compounds, as well as tubastatin A, we further studied their influence on apoptosis and cell cycle changes.

Table 3. Cytotoxic activities toward MDA-MB-231 and MCF-7 cell lines.

Compound	$IC_{50} \pm SD$ (μM)	
	MDA-MB-231	**MCF-7**
6b	33.40 ± 2.79	84.05 ± 5.2
7b	10.55 ± 1.95	>100
8b	5.42 ± 0.77	39.10 ± 2.7
9b	38.21 ± 3.01	99.50 ± 0.7
tubastatin A	20.83 ± 2.84	93.31 ± 9.4

Values are expressed as the mean ± SD of three independent experiments

2.2.3. **1-benzhydryl piperazine-based HDAC inhibitors induce translocation of cell membrane phosphatidylserine**

Initially, the ability of compounds to induce apoptosis of MDA-MB-231 cells were analyzed after 24, 48 and 72 h treatment at IC_{50} concentration by flow cytometry using Annexin V-FITC/7-AAD staining. Twenty-four hour treatment with **6b** and **7b** induced a slight increase in programmed cell death (Figure 4A). Following 48 h treatment we observed that all compounds induced almost the same percentage of early apoptotic cells (**Figure 4B**). Seventy-two hours treatment of MDA-MB-231 cells with **7b**, **8b** and **9b** at IC_{50} concentration

led to the strong increase in early apoptotic cell population (around 45%) (**Figure 4C**). Early apoptosis-inducing effects were time-dependent in treated MDA-MB-231 cells with the highest number of early apoptotic cells (approximately 45%) detected after 72 h of treatment (Figure 4C). The occurrence of early apoptosis (approximately 20 %) after MDA-MB-231 cells treatment with selective HDAC6 inhibitor **6b** was noticed after 48 and 72 h (**Figure 4B, C**). The percentage of early apoptotic cells increased gradually with increasing treatment duration with the selective HDAC6 inhibitor tubastatin A (**Figure 4 A-C**).
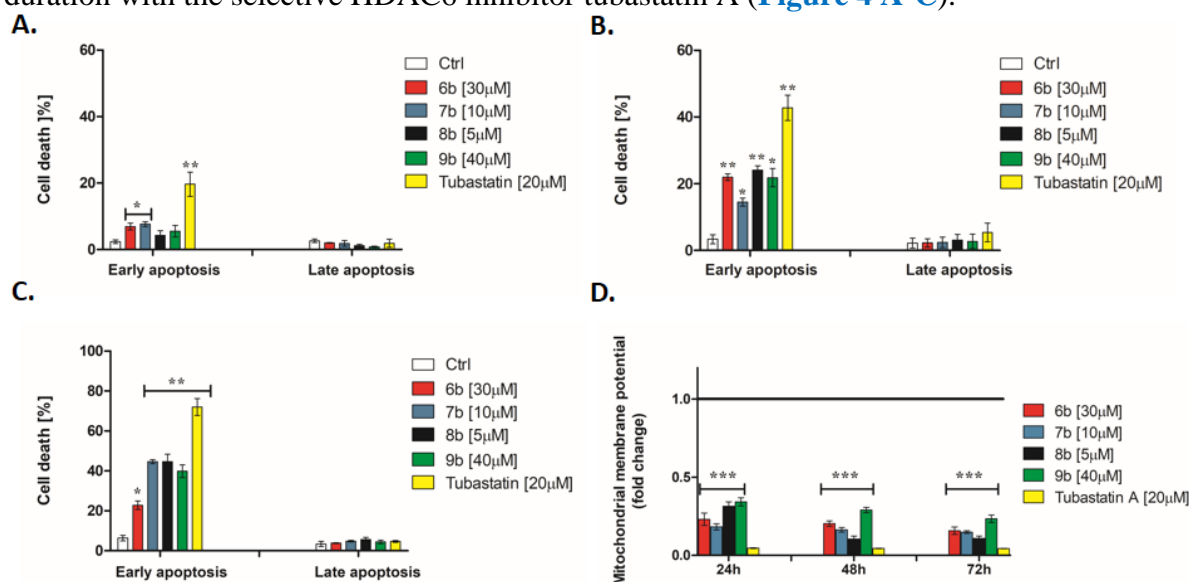

Figure 4. Newly synthesized HDAC inhibitors activate the intrinsic cell death pathway. The proportion of early apoptotic and late apoptotic MDA-MB-231 cells was measured using bivariate Annexin V/7AAD analysis by flow cytometry after the cells treatment with tested compounds at IC_{50} concentration for (**A**) 24 h, (**B**) 48 h and (**C**) 72 h. (**D**) Dissipation of mitochondrial membrane potential was assessed by flow cytometry using JC-1 dye (compared to the untreated control). A significant difference between treatments by t-test: *$p \leq 0.05$, **$p \leq 0.01$ (compared to the untreated control).

Anticancer drugs have been shown to activate the intrinsic apoptotic pathway.[42] One of the earliest changes in this process is the dissipation of mitochondrial membrane potential ($\Delta\psi$m)[43]. The flow cytometry data showed a dramatic loss of mitochondrial membrane potential ($\Delta\psi$m) in MDA-MB-231 cells even during 24 h treatment with all tested compounds (Figure 4D) indicating the initiation of mitochondrial apoptotic pathway program. Nevertheless, as our selective HDAC6 inhibitors do not induce significant apoptosis, we were interested in examining their effects on migration and invasion of MDA-MB-231 and MCF-7 breast cancer cells.

2.2.4. Intracellular ROS levels increased upon treatment with 9b

Reactive oxygen species (ROS) are highly reactive molecules that are considered as regulators in many signaling pathways in both normal and cancer cells. Elevated ROS levels can trigger programmed cell death which can be used as one of the strategies for eliminating cancer cells[44]. To examine the effect on the redox homeostasis of the tested HDAC inhibitors, an evaluation of the total level of endogenous ROS in treated breast cancer cells was performed. A significant increase in intracellular ROS accumulation was observed after the treatment of MDA-MB-231 cells with compound **9b**, especially after 24 h of treatment (Figure 5). On the other hand, other tested compounds showed a slight increase in intracellular ROS level in MDA-MB-231 cells after 48 h.
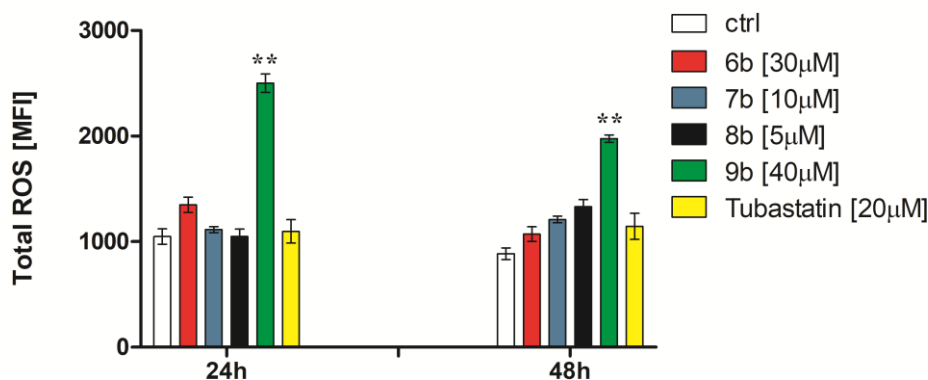
Figure 5. Increases of intracellular ROS level in the MDA-MB-231 cells upon treatments with **9b** at 24 h and 48h. The columns represent the total ROS level expressed as mean fluorescence intensity (MFI). A significant difference between treatments by t-test: **$p \leq 0.01$ (compared to the untreated control).

2.2.5. Treatment of MDA-MB-231 cells with inhibitors induce changes in the cell cycle

To account for possible anti-proliferative effects of synthesized HDAC inhibitors, we analyzed changes in the cell cycle distribution at IC_{50} concentrations in time-dependent manner. Treatment of MDA-MB-231 cells with all compounds resulted in a time-dependent increase of MDA-MB-231 dying cell population followed by the reduction of cells in G0/G1 phase of the cell cycle (Figure 6). Treatment of MDA-MB-231 cells with **7b** and **8b** at 24h resulted in a slight increase in the percentage of cells in the G2/M phase, while treatment with **9b** increases the percentage of cells in the S phase of the cell cycle (Figure 6). Also, the treatment of cells with **7b**, **8b** and 9b after 48 h increased percentage of cells in S phase (Figure 6). Tubastatin A increases of MDA-MB-231 dying cell population (sub-G1 phase cells around 30% at 72h) in time-dependent manner followed by the reduction of cells in the G0/G1 phase of the cell cycle (Figure 6).
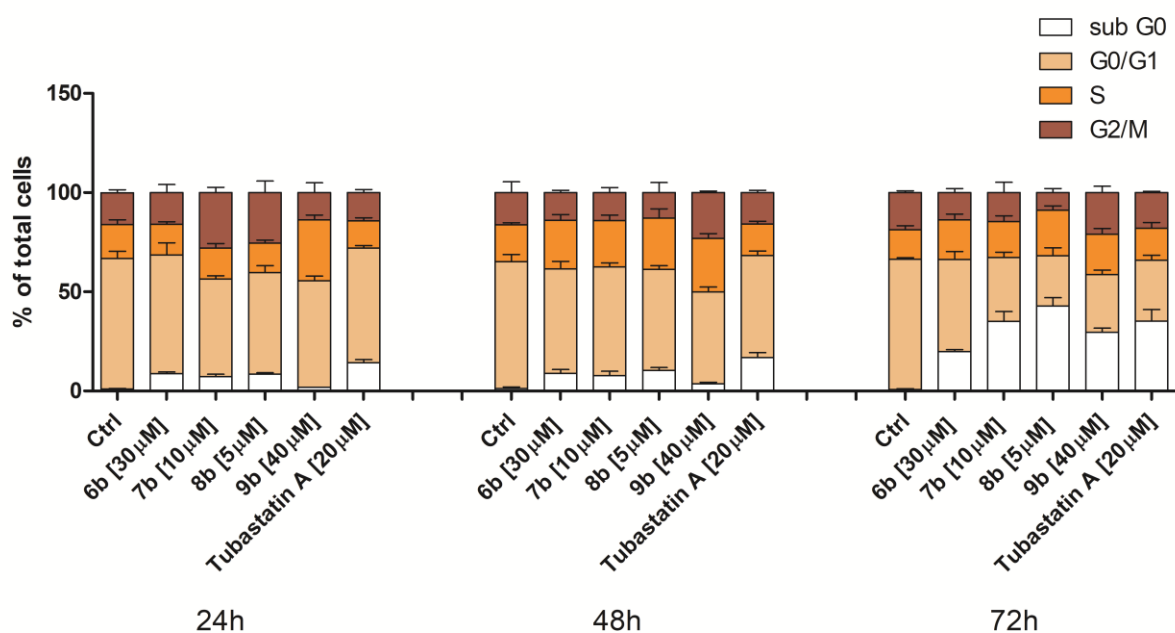
Figure 6. Changes in cell cycle phase distribution of MDA-MB-231 cells upon treatment with compounds **6b, 7b, 8b, 9b and tubastatin A**. After the 24h, 48h and 72h continual treatment of MDA-MB-231 cells with **investigated compounds** at IC$_{50}$ concentration, as well as tubastatin A at IC$_{50}$ 20 μM, cells were stained with propidium iodide and analyzed by flow cytometry. White bar - apoptotic cells with DNA content corresponding to sub-G1 fraction; sandy bar - cells with DNA content corresponding to G0/G1 phases; orange bar - cells with DNA content corresponding to S phase; maroon bar - cells with DNA content corresponding to G2/M phases (compared to the untreated control).

2.2.6. Analyses of the efficacy of compounds in a 3D cancer model

Three-dimensional (3D) cell cultures may mimic the natural *in vivo* setting more representative than 2D cultures since 3D models are beginning to restore the cellular morphologies, phenotypes, and interactions seen during *in vivo* tumor development[45].
A 3D tumor sphere model, of MDA-MB-231 cells, was introduced to investigate the effects of synthesized compounds at the equimolar concentration (50 μM) on the viability and growth kinetics of tumor spheres after 72h, in comparison to tubastatin A. After 4 d, formed spheres treated with **8b** for 72 h revealed tenfold lower sensitivity to **8b** (IC$_{50}$=50 μM) (Figure 7 B) than in 2D cell culture (Table 1). Compound **6b**, as well as **tubastatin A,** caused a mild decrease in tumor spheres viability at 50 μM concentration, while compounds **7b** and **9b** did not exhibit significant cytotoxic effects in examined spheres (Figure 7B). Also, **8b**-treated spheres decreased in size after 72 h treatment (Figure 7A).
Next, a testing of the ability of compounds to inhibit the tumor sphere formation was performed. MDA-MB-231 cells were co-cultured with the compounds (IC$_{50}$ and 50 μM) in sphere culture conditions for 4 d (Figures 7C and D). After 4 d, untreated cells formed spheres that had a tightly packed morphology (Figure 7C). Meanwhile, the incubation of MDA-MB-231 cells with **8b** and **tubastatin A** (50 μM) for 4 d in sphere culture conditions, significantly inhibited both sphere formation and spheres viability (Figures 7C and D). In turn, compounds **6b** and **7b**, at higher concentrations inhibit sphere formation to some extent (Figure 7 C and D).
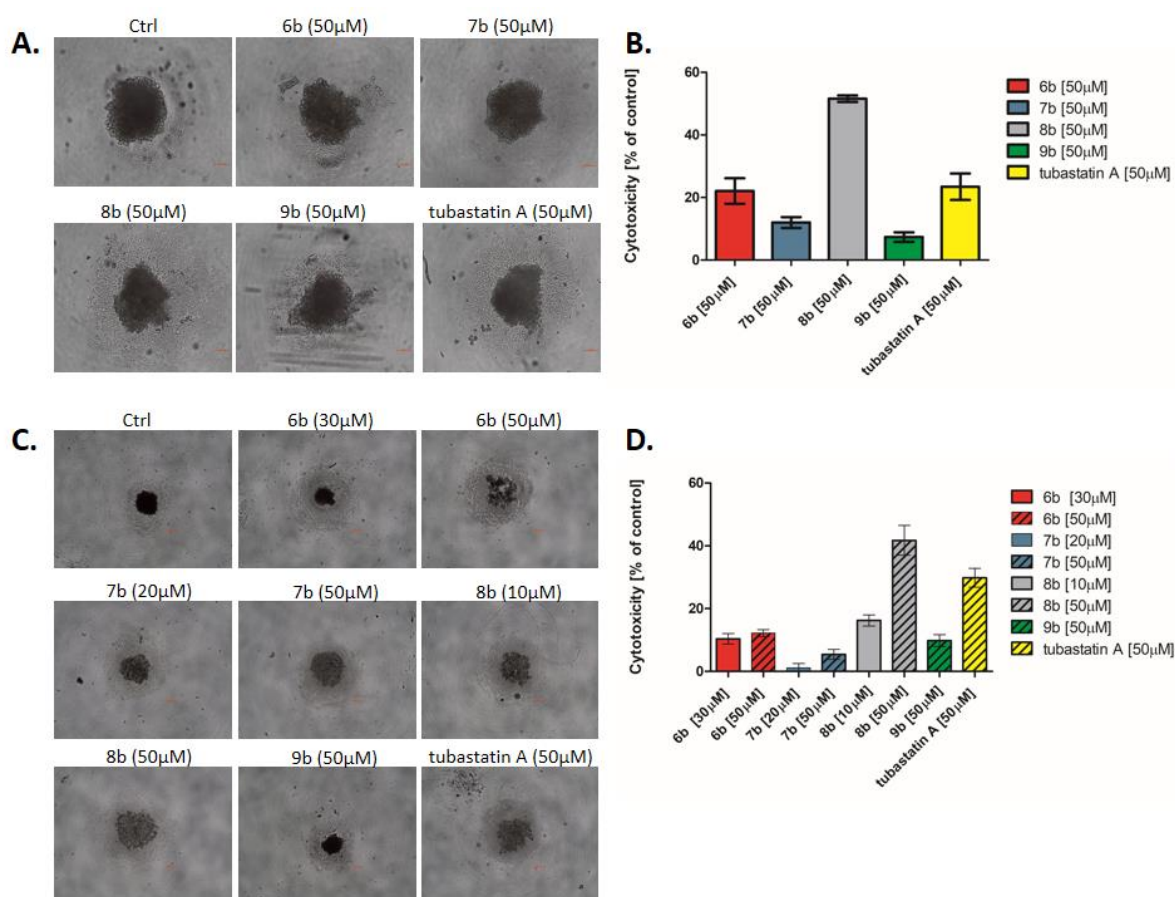
Figure 7. Inhibition of cell survival and growth of MDA-MB-231 tumor spheroids treated with synthesized compounds. After 4 d, formed spheres were treated with synthesized compounds and tubastatin A at equimolar concentration (50μM) for 72 h. The formation and growth of tumor spheres were examined and imaged with an Olympus CKX53, using 4x/0.13 and 10x/0.25objective, scale bar:100 μM. (**A**) MDA-MB-231 tumor spheroids observed under the bright field, and (**B**) the cytotoxicity of compounds toward the MDA-MB-231 tumor spheres was investigated by MTT assay. (**C**) MDA-MB-231 cells were co-cultured with the tested compounds (IC$_{50}$ and 50 μM) in sphere culture conditions for 4 d. The formation and growth of tumor spheres were examined and imaged with an Olympus CKX53, using 4x//0.4 objective, scale bar: 200 μM. (D) the cytotoxicity of compounds in the co-treatment with MDA-MB-231 tumor spheres was investigated by MTT assay.

2.2.7. 8b decreases migration and invasion of triple-negative breast cancer MDA-MB-231 cell-line *in vitro*.

One of the hallmarks of cancer cell malignancy is the acquisition of cell motility that allow the cancer cell to migrate and invade neighboring tissues and organs. As our selective HDAC6 inhibitors do not induce significant apoptosis, we were interested in examining their effects on migration and invasion of MDA-MB-231 and MCF-7 breast cancer cells. Chemically similar **8b** (nonselective HDAC inhibitor) and **9b** (selective HDAC6 inhibitor) were selected to be compared in terms of anti-migratory and anti-invasive properties. Two related *in vitro* assays were employed: a transwell migration, that mimics cell movement from one culture compartment by crossing through a membrane with 8 μm pores to another; and cell invasion, in which the membrane is coated with a layer of Matrigel that represents a tumor extracellular matrix (ECM), and cells display proteolytic functions to cross trough the

ECM among others[46,47]. MDA-MB-231 cells were subjected to migration and invasion *in vitro* analyses and treated with 5 μM **8b** and 10 μM **9b** for a period of 24 h. To perform the transwell migration and invasion assays with viable cells during the time course of experiments, these concentrations were selected according to the apoptosis analysis by flow cytometry (Figure S9, Supp. Info). As shown in **Figure 8A**, only **8b** exerts anti-migratory (68% compared to control) and anti-invasive (59% compared to control) properties, as demonstrated by the reduced capacity of MDA-MB-231 cells to move across the transwells to the bottom of membranes in both migration and invasion assay (Figure 8B). Meanwhile, **9b** did not alter MDA-MB-231 cancer cell migration and invasion compared to control cells in our experimental conditions.
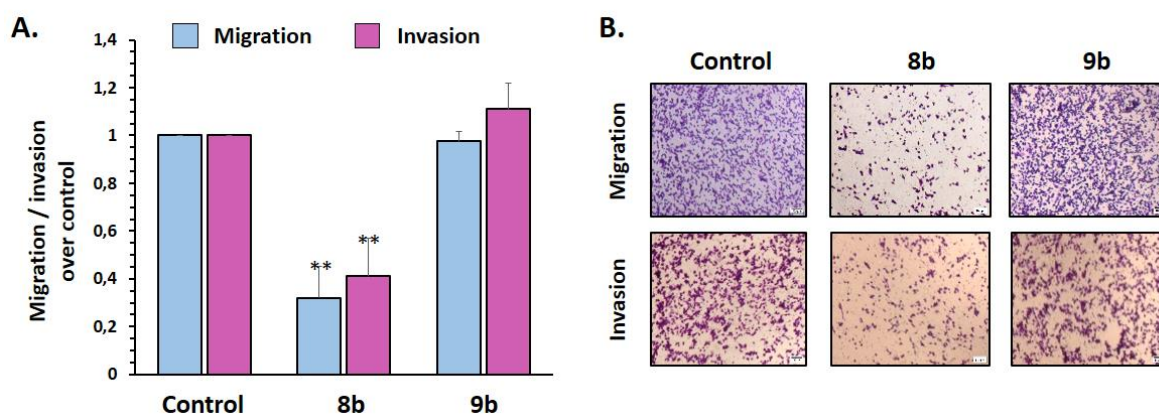

Figure 8. 8b inhibits migration and invasion of MDA-MB-231 cells (A); MDA-MB-231 cells were subjected to bicameral migration (blue) and invasion (purple) assay. Cells were treated with 5 μM of **8b** and 10 μM of **9b** for 24 h. Cells in the bottom of the 8 mm pore membrane were fixed and quantified. Microphotographs are shown crystal violet stained migratory and invasive cells (B). Magnification 40X, bar=50 μm. Representative results from three independent experiments are shown. Significant difference between treatments by t-test: $**p < 0.01$.

Although HDAC6 has been postulated to play roles in the migration and invasion of cancer cells, mainly by influencing tubulin acetylation and microtubules dynamics[18,48], the use of **9b**, at concentrations of seven-fold below the IC_{50}, failed to inhibit the TNBC MDA-MB-231 cells migration and invasion. Whether MDA-MB-231 tubulin cytoskeleton is refractory to HDAC6 inhibition is a matter of future analysis. Nonetheless, an association between estrogen receptor alpha (ERα) and HDAC6 is necessary for the deacetylation of tubulin and increased migration in breast cancer cells[49,50]. This evidence is consistent with the inhibition of **9b** of ER+ MCF-7 cell-line migration (63.9% inhibition of the wound closure compared to control) determined by wound-healing assay (Figure S10, Supp. Info).

2.2.4. Toxicity assessment *in vivo* using the zebrafish model

In order to address whether the most potent newly-synthesized HDACi **8b** and **9b** could be applied to humans, we used the zebrafish (*Danio rerio*) as a pre-clinical animal model and examined acute and inner organs toxicity upon the applied molecules. The zebrafish has emerged as a universal biotechnological platform for effective and safe drug discovery owing to their genetic, molecular, and immunological similarity to humans, and highly correlated response to pharmaceuticals including anti-cancer compounds[51–53]. The use of this model system simplifies the path of novel bioactive compounds to clinical trials and reduce the failure of potential therapeutics at later stages of testing[54,55].

Here, we found that none of the two novel HDACi caused lethal effect at doses up to 100 μM after the 5-day treatment (LC$_{50}$ >100 μM) (Fig. 9A). The data obtained in this assay showed better toxicology profile of **8b** compared to **9b**. While none embryos exposed to 50 μM of **8b** showed signs of teratogenicity, cardio- and hepatotoxicity (Fig. 9B), 32% embryos treated with **9b** were teratogenic (malformed head, jaw, body), had pericardial edema, and necrotic and small liver. Interestingly, the embryos exposed to 25 and 50 μM of **8b** had reduced circulation in the caudal region indicating the possible inhibition of angiogenesis by the applied molecule.
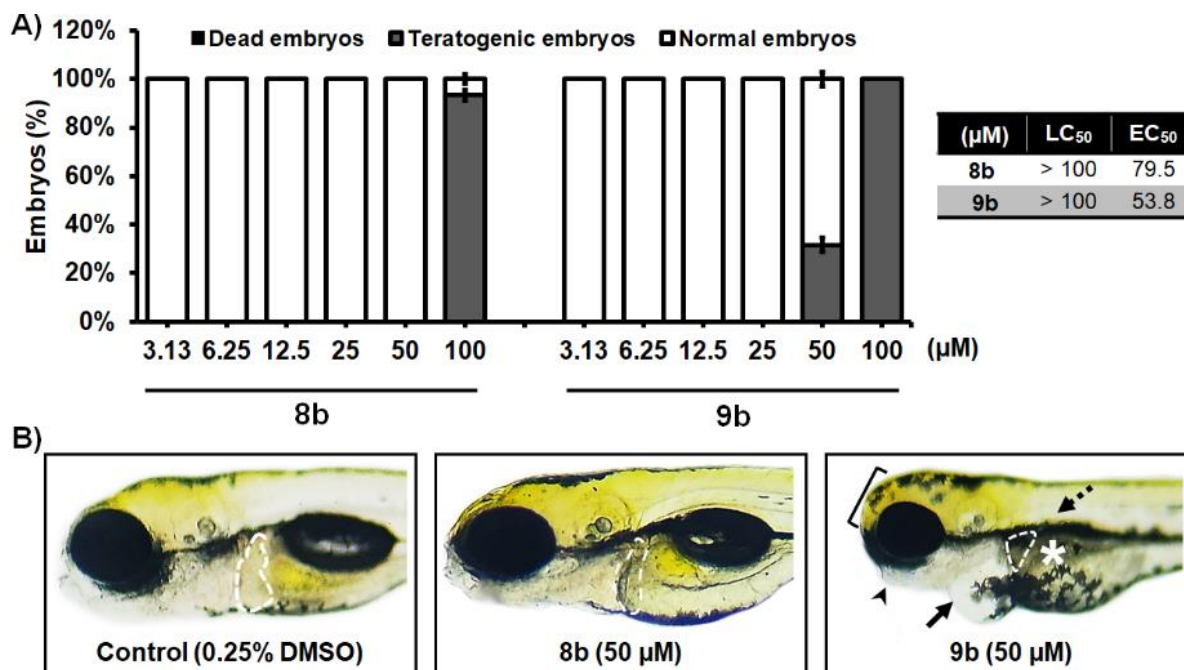

Figure 9. *In vivo* toxicity assessment of 1-benzhydryl piperazine-based HDAC inhibitors **8b** and **9b** in the zebrafish (*Danio rerio*) model. A) Acute toxicity was assessed using wild type (AB) embryos exposed to different doses of tested molecules, and expressed as the LC$_{50}$ and EC$_{50}$ doses. Embryos were treated at 6 h post fertilization (hpf) and evaluated for survival, teratogenicity, cardiotoxicity and hepatotoxicity at 120 hpf (n = 60 per a dose). B) Embryos exposed to 50 μM of **8b** were normally developed embryos, without signs of cardiotoxicity, hepatotoxicity and teratogenicity. On the other side, treatment with **9b** in some embryos provoked pericardial edema (arrow), weakly resorbed yolk (asterisk), malformed head (bracket) and jaw (arrowhead), no inflated swim bladder (dashed arrow) and decreased and dark liver (outlined). No adverse effect on the liver was detected at 50 μM of **8b,** while reduced liver size and darkening (necrosis) occurred in embryos exposed to 50 μM od **9b.**

2.2.5. Anti-angiogenic effects of 8b and 9b on developing zebrafish

Prompted by the observation of reduced circulation in zebrafish embryos treated with **8b**, we explored the capability of this HDAC inhibitor to inhibit the process of neoangiogenesis *in vivo*, which is a prerequisite for the cancer growth, invasion, and metastasis[56]. While controllable and balanced angiogenesis is essential for normal physiological processes, excessive angiogenesis is important for tumor development and tumor cell metastasis[56]. Accordingly, the inhibition of new blood vessel formation is a proven clinical strategy for treating solid tumors, which combined with cytostatic noticeably increases the efficacy of chemotherapy and provides significantly better survival rate of the cancer patients[57].

Here, the suppression of angiogenesis was studied using transgenic zebrafish $Tg(fli1$:EGFP) embryos, which the endothelial cells express EGFP enabling us to directly assess the effect of the applied HDAC inhibitor on the vessels development upon fluorescence microscopy. Embryos were exposed to **8b** doses ranging from 6.25 to 50 µM (corresponding to non-toxic doses) and imaged for intersegmental vessels (ISVs) development after 48 h of treatment. In normally developing embryos, 28–30 ISVs were present. The anti-angiogenic phenotype was defined as the reduced number and/or length of ISVs along the whole body. As shown in Figure 10, **8b** effectively inhibited the ISV angiogenesis in a dose-dependent manner. The treated embryos displayed anti-angiogenic phenotype already at the **8b** dose of 6.25 µM and ~60% of the embryos were affected in the ISV vessels growth (Figure 10B, P <0.05, χ^2 test); on the other side, the majority of ISV vessels were inhibited at 25 and 50 µM doses of **8b** (Figures 10C and 10D). It is important to emphasize that the treatment with the effective doses of **8b** did not elicit any toxic response in the treated embryos, indicating its safety at anti-angiogenic regime. On the other side, sunitinib-malate (Suten), a clinical anti-angiogenic drug, provoked life-threatening pericardial edema (Figure 10A) what progressively decreased the embryos' survival by 120 hpf (data not shown). Toxicity issues, in particular cardiotoxicity, limit the clinical use of sunitinib at its higher doses and for prolonged period of time, what restricts its overall anti-angiogenic potential and efficacy of applied therapy[58].
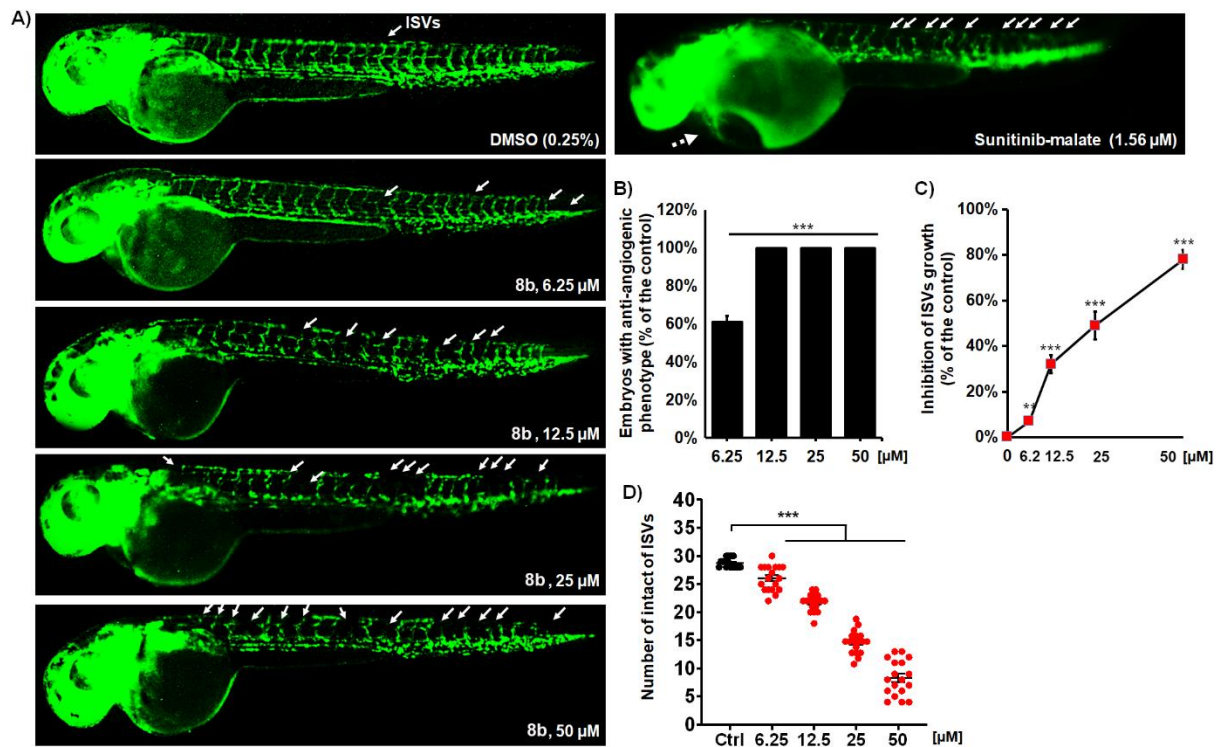

Figure 10. 8b effectively inhibits angiogenesis in $Tg(fli1$:EGFP) zebrafish embryos with fluorescently labelled endothelial cells. Embryos were exposed to the four doses of **8b** and assessed for the inhibition of ISV vasculature at 48 hpf (A). Treatment with **8b** increased number of embryos with anti-angiogenic phenotype (B), decreased the number of normally developed ISV vessels (C) and reduced the ISVs length (D) in the dose-dependent manner. Sunitinib-malate (Suten), a clinically approved anti-angiogenic drug, was used as a positive control. While the Suten caused life-threating cardiotoxicity at the effective dose of 1.56 µM, **8b** inhibited angiogenesis without any toxic response in the treated embryos. Representative images of embryos are shown. Data are normalized in relation to the control group (B, C).

Significance in the analyzed parameters between **8b** treated embryos and control (DMSO-treated) embryos is indicated with asterisks (**$P < 0.01$; ***$P < 0.001$).

2.2.6. 8b inhibits MDA-MB-231 breast tumor development and successfully prevents tumor cell metastasis

The data on potent inhibition of MDA-MB-231 cell migration and invasion *in vitro* (Figure 8) justified evaluation of the anti-metastatic activity of **8b** *in vivo*. We used the zebrafish-MDA-MB-231 xenograft model and examined the effect of the applied HDACi on tumor development and tumor cell metastasis. Zebrafish xenografts represent a powerful platform for translational research in human carcinomas demonstrating the crucial hallmarks of cancer biology such as tumor cell proliferation, dissemination, metastasis, extravasation and tumor-driven angiogenesis[59]. The use of this model provides differential discrimination on anti-cancer therapy efficacy with single-cell resolution[60]. Accordingly, MDA-MB-231 cells were fluorescently labelled and injected into the yolk of *Tg*(*fli1*:EGFP) embryos. At 3 days post treatment (dpt), MDA-MB-231 xenografts were processed for fluorescence microscopy and examined for the effect of **8b** treatment on tumor mass development and cancer cells dissemination and metastasis.

The results obtained in this assay revealed that the treatment with **8b** inhibited both MDA-MB-231 tumor mass development ($P < 0.001$; Figure 11B) and cancer cell dissemination (Figure 11C, 11D; $P < 0.001$). Compared to the tumor mass developed in the untreated (control) embryos after 3 days post injection, **8b** reduced mass of breast carcinoma by $56.1 \pm 5.2\%$ at 3.13 µM dose, while almost complete reduction was achieved at 12.5 µM ($P < 0.001$ for both doses; Figures 11A and 11B). Remarkably, no toxic side effects were observed in the xenografts receiving **8b** treatment what is of a particular relevance since many clinically approved anti-cancer drugs are cardio- and hepatotoxic that limit their long-term application in chemotherapy. Analysis of the data for the tumor mass inhibition after the day treatment we determined the ED_{50} of **8b** (effective drug concentration reducing tumor mass by 50% in relation to the control) was 2.67 µM. Considering that LC_{50} for **8b** was >100 µM, this is evidence that this HDACi possesses a large therapeutic window (determined as the LC_{50}/ED_{50} ratio) and clearly indicates that **8b** is a novel, perspective anti-cancer molecule.
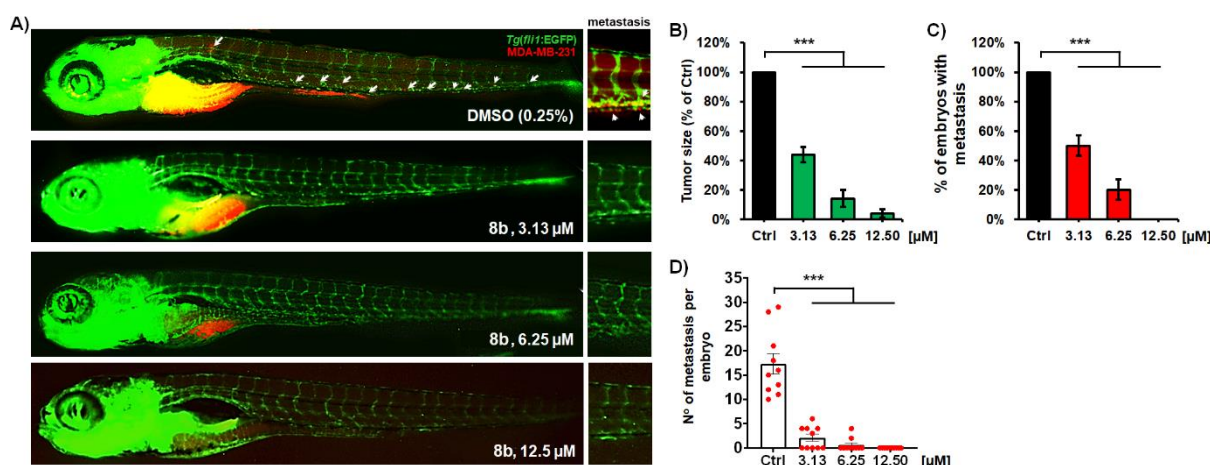

Figure 11. Anti-cancer and anti-metastatic activity of a new HDAC inhibitor **8b** against highly metastatic human breast carcinoma MDA-MB-231 cells in zebrafish xenografts. *Tg*(*fli1*:EGFP) xenografts (n = 20) were exposed to three different doses of **8b**, and analysed for tumour progression and metastasis after 3-day treatment. Representative fluorescent microscopy images are shown (**A**); white arrows indicate disseminated cells. The applied treatments markedly reduced the MDA-MB-231 tumor growth (**B**), number of embryos with

metastasis (**C**) as well as the number of disseminated cancer cells per xenograft (**D**), as compared to those in the control group (P <0.001, for all hallmarks). Data are normalized in relation to the control group (B, C***P <0.001).

In addition to anti-tumor effect, the newly synthesized HDACi **8b** exhibited very potent anti-metastatic activity (Figures 11C, 11D). Dissemination of MDA-MB-231 cancer cells through the body of xenografts was significantly reduced at **8b** dose of 3.13 μM. In comparison to the untreated xenografts, the number of embryos having metastases was reduced by 50% (Figure 11C) and the number of metastasis per embryos was up to 9.6-fold lower (Figure 11D) after 3-days treatment with 3.13 μM **8b**. Moreover, fluorescence microscopy showed that dissemination of MDA-MB-231 cells was completely inhibited at 12.5 μM of **8b** (Figure 11A). It is also important to note that the ISV vasculature of MDA-MB-231 xenografts stayed functional and visible during the entire treatment with **8b** what indicates that: i) applied treatment has no negative effect on established vasculature, ii) existing vasculature provides nutrient supply to tumor cells and their dissemination, and iii) inhibition of tumor cells dissemination was not due to the existing vasculature impairment but due to anti-metastatic activity of **8b**.

3. Conclusion

In this work, 1-benzhydryl-piperazine was employed as a novel surface-recognition (CAP) group to design potent HDAC6 inhibitors with anti-metastatic effects in breast cancer. A batch of 8 hydroxamic acid derivatives of 1-benzhydryl-piperazine was synthesized by varying the nature of hydrocarbon linker. Two novel selective HDAC6 inhibitors (**6b**, IC_{50}=186 nM and **9b**, IC_{50}=31 nM) were identified, exhibited more than 10 to 110-fold selectivity over nuclear isoforms HDAC1/3/8. Both potency and selectivity profiles of synthesized selective HDAC6i are comparable with the clinical drug candidates ricolinostat and citarinostat. The analogues with 6 and 7 carbon atoms in the linker (**7b** and **8b**) were associated with nanomolar potencies, but were nonselective HDACi. The preliminary SAR analysis supported with structure-based molecular modelling suggested that five-carbon atoms (**6b**) is optimal linker length for achieving selective HDAC6 inhibition among the group of alkyl-hydroxamic acid derivatives. Phenyl-hydroxamic acid derivative (**9b**) demonstrated superior HDAC6 selectivity profile among other synthesized 1-benzhydryl piperazine derivatives.

Evaluation of anti-cancer effects in breast cancer cells (MDA-MB-231 and MCF-7) indicated that the primary mechanism of action of **8b** involves apoptosis via loss of mitochondrial membrane potential. Contrary to these, selective HDAC6 inhibitors (**6b** and **9b**) induced apoptosis after 72 h treatment that could be explained by inhibition of nuclear HDAC isoforms after prolonged incubation. **8b** effectively decreases the migratory and invasive potential of triple-negative breast cancer cell-line (MDA-MB-231), whereas **9b** shows anti-migratory effect in wound-healing assay toward MCF-7 cell-line. With better *in vivo* toxicology profile, **8b** inhibits formation of novel intersegmental vessels (ISV) at 6.25 μM and potently reduces the growth (ED_{50} = 2.67 μM) and dissemination of MDA-MB-231 cells in zebrafish-MDA-MB-231 xenograft model. To conclude, **8b** is a novel epigenetic inhibitor and a promising small molecule valuable for further preclinical development as potential breast cancer therapeutics.

4. Experimental section

4.1. Chemistry – general procedures

All chemicals and solvents were purchased from commercial sources and were used without further purification. ^{1}H and ^{13}C nuclear magnetic resonance (NMR) spectra were recorded on a Bruker Ascend 400 (400 MHz) spectrometer at room temperature, using TMS as an internal standard. Chemical shifts were reported in ppm (δ). Spin multiplicities were described as s (singlet), d (doublet), dd (double doublet), t (triplet), or m (multiplet). Coupling constants were reported in hertz (Hz). Mass spectral data were recorded using an Agilent Technologies 6520 Q-TOF spectrometer coupled with an Agilent 1200 HPLC, LTQ Orbitrap XL by electrospray ionization (ESI).

4.2. Alkylation of 1-benzhydryl piperazine (General Procedure A)

In a round bottom flask the 1 equivalent of 1-benzhydryl piperazine was dissolved in acetonitrile (5 mL), 1.1 equivalents of corresponding bromo-methyl ester was added along with 1.7 equivalents of potassium carbonate at 0 °C. The reaction mixture was heated under reflux overnight. The completion of the reaction was followed by TLC (ethyl acetate: dichloromethane = 1:1). When the reaction was completed, the mixture was filtered through Celite and washed with ethyl acetate. The solvents were removed *in vacuo*, and the mixture was purified with Flash chromatography.

4.2.1. *Methyl [4-(diphenylmethyl)-1-piperazinyl]acetate (2a).* Brownish oil (369.2 mg, yield 54%). ^{1}H NMR (400 MHz, CDCl$_3$): δ 7.40 (d, J = 7.3 Hz, 4H), 7.26 (t, J = 7.5 Hz, 4H), 7.16 (t, J = 7.3 Hz, 2H), 4.24 (s, 1H), 3.70 (s, 3H), 3.22 (s, 2H), 2.60 (s, 4H), 2.46 (s, 4H). ^{13}C NMR (101 MHz, CDCl$_3$): δ 170.7, 142.6, 128.4, 127.9, 126.9, 76.1, 59.4, 53.3, 51.6, 51.6.

4.2.2. *Methyl 3-[4-(diphenylmethyl)-1-piperazinyl]propanoate (3a).* Brownish oil (224.6 mg, yield 66%). ^{1}H NMR (400 MHz, CDCl$_3$): δ 7.39 (d, J = 7.4 Hz, 4H), 7.23 (t, J = 7.5 Hz, 4H), 7.14 (t, J = 7.3 Hz, 2H), 4.20 (s, 1H), 3.63 (s, 3H), 2.68 (t, J = 7.4 Hz, 2H), 2.45 (m, 10H). ^{13}C NMR (101 MHz, CDCl$_3$): δ 172.8, 142.7, 128.4, 127.8, 126.8, 76.1, 53.4, 53.1, 51.8, 51.4, 32.1.

4.2.3. *Methyl 4-[4-(diphenylmethyl)-1-piperazinyl]butanoate (4a).* Pale yellow powder (300.0 mg, yield 85%). ^{1}H NMR (400 MHz, CDCl$_3$): δ 7.40 (d, J = 7.4 Hz, 4H), 7.25 (t, J = 7.5 Hz, 4H), 7.16 (t, J = 7.3 Hz, 2H), 4.21 (s, 1H), 3.64 (s, 3H), 2.45 (s, 6H), 2.33 (m, 6H), 1.79 (m, 2H). ^{13}C NMR (101 MHz, CDCl$_3$): δ 173.9, 142.8, 128.4, 127.9, 126.8, 76.2, 57.6, 53.3, 51.9, 51.4, 32.1, 22.2.

4.2.4. *Methyl 5-[4-(diphenylmethyl)-1-piperazinyl]pentanoate (5a).* Light brown oil (248.2 mg, yield 67%). ^{1}H NMR (400 MHz, CDCl$_3$): δ 7.40 (d, J = 7.3 Hz, 4H), 7.25 (t, J = 7.5 Hz, 4H), 7.16 (t, J = 7.3 Hz, 2H), 4.21 (s, 1H), 3.65 (s, 3H), 2.44 (s, 7H), 2.32 (m, 5H), 1.63 (m, 2H), 1.49 (m, 2H). ^{13}C NMR (101 MHz, CDCl$_3$): δ 174.0, 142.8, 128.4, 127.95, 126.8, 76.2, 58.1, 53.5, 51.9, 51.4, 33.9, 26.3, 23.0.

4.2.5. *Methyl 6-[4-(diphenylmethyl)-1-piperazinyl]hexanoate (6a).* White powder (235.55 mg, yield 78%). ^{1}H NMR (400 MHz, CDCl$_3$): δ 7.41 (d, J = 7.3 Hz, 4H), 7.28 (t, J = 7.5 Hz, 4H), 7.17 (t, J = 7.3 Hz, 2H), 4.24 (s, 1H), 3.57 (s, 3H), 2.35 (s, 4H), 2.28 (t, J = 7.4 Hz, 4H), 2.24 – 2.08 (m, 4H), 1.56 – 1.46 (m, 2H), 1.43 – 1.32 (m, 2H), 1.30 – 1.18 (m, 2H). ^{13}C NMR (101 MHz, CDCl$_3$): δ 173.7, 143.4, 128.9, 128.0, 127.2, 75.7, 58.1, 53.3, 52.0, 51.5, 33.7, 26.9, 26.4, 24.8.

4.2.6. *Methyl 7-[4-(diphenylmethyl)-1-piperazinyl]heptanoate (7a).* Pale yellow powder (289.2 mg, yield 73%). ^{1}H NMR (400 MHz, CDCl$_3$): δ 7.41 (d, J = 7.7 Hz, 4H), 7.25 (m, 4H), 7.16 (t, J = 7.2 Hz, 2H), 4.21 (s, 1H), 3.65 (d, J = 1.8 Hz, 3H), 2.44 (s, 7H), 2.34 – 2.23 (m, 5H), 1.64 – 1.58 (m, 2H), 1.46 (s, 2H), 1.30 (d, J = 3.1 Hz, 4H). ^{13}C NMR (101 MHz, CDCl$_3$): δ 174.1, 142.8, 128.4, 127.9, 126.8, 76.2, 58.6, 53.5, 51.9, 51.4, 34.0, 29.0, 27.2, 26.7, 24.8.

4.2.7. *Methyl 8-[4-(diphenylmethyl)-1-piperazinyl]octanoate (8a).* Crystalline white powder (362.7 mg, 60% yield). ^{1}H NMR (400 MHz, DMSO) δ 7.40 (d, J = 7.3 Hz, 4H), 7.27 (t, J = 7.5 Hz, 4H), 7.16 (t, J = 7.3 Hz, 2H), 4.23 (s, 1H), 3.56 (s, 3H), 2.34 (s, 6H), 2.34 – 2.17 (m, 6H), 1.55 – 1.45 (m, 2H), 1.36 (s, 2H), 1.23 (s, 6H). ^{13}C NMR (101 MHz, DMSO) δ 173.8, 143.4, 128.9, 128.0, 127.2, 75.7, 58.2, 53.4, 52.0, 51.5, 33.7, 29.0, 28.8, 27.2, 26.6, 24.8.

4.2.8. *Methyl 4-[4-(diphenylmethyl)-piperazin-1-ylmethyl]benzoate (9a)*. Crystalline brown powder (398.0 mg, 99% yield). ^{1}H NMR (400 MHz, CDCl$_3$): δ 8.01 – 7.93 (m, 2H), 7.44 – 7.35 (m, 6H), 7.30 – 7.21 (m, 4H), 7.16 (m, 2H), 4.23 (d, J = 5.3 Hz, 1H), 3.88 (d, J = 2.0 Hz, 3H), 3.55 (d, J = 2.8 Hz, 2H), 2.47 (s, 8H). ^{13}C NMR (101 MHz, CDCl$_3$): δ 167.0, 142.7, 129.5, 128.9, 128.4, 127.9, 126.8, 76.1, 62.6, 53.4, 51.9, 51.8.

4.3. *Synthesis of hydroxamic acid derivatives (General Procedure B)*

Freshly prepared solution of hydroxylamine in methanol was made by mixing methanol solutions of hydroxylamine hydrochloride (3 equivalents) and potassium hydroxide (6 equivalents). The mixture was rigorously stirred on ice bath for 30 min during which potassium chloride precipitate was formed. The precipitate was removed by filtration and freshly prepared NH$_2$OH was used for synthesis of hydroxamic acids derivatives.

To a solution of corresponding methyl-ester **2a-9a** (1 equivalent) dissolved in MeOH and cooled at 0 °C, freshly prepared methanol NH$_2$OH solution (3 equivalents) was added dropwise. The pH of solution was adjusted with KOH to be approximately 10. The mixture was left to stir at room temperature for 4-6 h. After completion of reaction, methanol was evaporated, saturated solution of NaHCO$_3$ was added and the hydroxamic acid derivative was washed with ethyl acetate. The compound was washed with brine (3×5 mL) and dried over anhydrous Na$_2$SO$_4$. The organic solvent was removed under reduced pressure. Purification by flash column chromatography (dichloromethane:methanol=95:5) afforded the desired hydroxamic acid derivatives.

4.3.1. *2-(4-(diphenylmethyl)-piperazin-1-yl)-N-hydroxyacetamide (2b)*. Yellow brownish oil (118.6 mg, 41% yield). ^{1}H NMR (400 MHz, MeOD) δ 7,42 (d, J = 7,5 Hz, 4H), 7,25 (t, J = 7,5 Hz, 4H), 7,16 (t, J = 7,3 Hz, 2H), 4,23 (s, 1H), 3,01 (s, 2H), 2,70 (d, J = 4,8 Hz, 2H), 2,55 (s, 3H), 2,43 (s, 3H). ^{13}C NMR (101 MHz, MeOD) δ 166.1, 141.1, 126.5, 126.0, 125.1, 74.7, 57.3, 51.5, 49.84. HRMS (ESI) calcd for C$_{19}$H$_{23}$N$_3$O$_2$ [M + H]$^+$: 326.1863, Found: 326.1866.

4.3.2. *3-(4-(diphenylmethyl)-piperazin-1-yl)-N-hydroxypropionamide (3b)*. Brown oil (30.1 mg, 18% yield). ^{1}H NMR (400 MHz, MeOD) δ 8.55 (s, 1H), 7.42 (d, J = 7.4 Hz, 4H), 7.26 (t, J = 7.5 Hz, 4H), 7.16 (t, J = 7.3 Hz, 2H), 4.23 (s, 1H), 2.67 (t, J = 7.3 Hz, 2H), 2.53 (s, 4H), 2.43 (s, 4H), 2.29 (t, J = 7.3 Hz, 2H).^{13}C NMR (101 MHz, MeOD) δ 169.9, 142.6, 128.1, 127.5, 126.6, 76.2, 53.5, 52.6, 51.3, 29.7. HRMS (ESI) calcd for C$_{20}$H$_{25}$N$_3$O$_2$ [M + H]$^+$ 340.1947, Found: 340.2020.

4.3.3. *4-(4-(diphenylmethyl)-piperazin-1-yl)-N-hydroxybutyramide (4b)*. Brownish oil that crystallizes in the fridge (39.0 mg, 27% yield). ^{1}H NMR (400 MHz, MeOD) δ 7.45 (d, J = 7.4 Hz, 4H), 7.30 (t, J = 7.5 Hz, 4H), 7.20 (t, J = 7.3 Hz, 2H), 4.38 (s, 1H), 3.35 (s, 1H), 3.20 (s, 3H), 3.07 (t, J = 6.3 Hz, 2H), 2.63 (s, 4H), 2.46 – 2.39 (m, 2H), 1.93 – 1.83 (m, 2H). ^{13}C NMR (101 MHz, MeOD) δ 178.7, 141.7, 128.4, 127.5, 127.1, 74.9, 57.3, 51.8, 48.9, 35.0, 19.7. HRMS (ESI) calcd for C$_{21}$H$_{27}$N$_3$O$_2$ [M + H]$^+$ 354.2176, Found: 354.2224.

4.3.4. *5-(4-(diphenylmethyl)-piperazin-1-yl)-N-hydroxypentanamide (5b)*. Dark brown oil (42.0 mg, 43% yield). ^{1}H NMR (400 MHz, MeOD) δ 7.40 (d, J = 7.5 Hz, 4H), 7.24 (t, J = 7.5 Hz, 4H), 7.15 (t, J = 7.3 Hz, 2H), 4.29 (s, 1H), 3.06 (s, 4H), 2.87 (d, J = 6.9 Hz, 2H), 2.57 (s, 4H), 2.19 (s, 2H), 1.71 – 1.52 (m, 4H). ^{13}C NMR (101 MHz, MeOD) δ 179.7, 141.9, 128.4, 127.4, 127.0, 75.2, 56.1, 51.8, 48.9, 35.9, 23.6, 22.7. HRMS (ESI) calcd for C$_{22}$H$_{29}$N$_3$O$_2$ [M + H]$^+$ 368.2333, Found:368.2337.

4.3.5. *6-(4-(diphenylmethyl)-piperazin-1-yl)-N-hydroxyhexanamide (6b)*. White crystalline powder (64.2mg, 64%. yield). ^{1}H NMR (400 MHz, DMSO) δ 7.40 (d, J = 7.5 Hz, 4H), 7.27 (t, J = 7.6 Hz, 4H), 7.16 (t, J = 7.3 Hz, 2H), 4.24 (s, 1H), 2.32 (d, J = 25.7 Hz, 7H), 2.23 – 2.19 (m, 2H), 2.11 (t, J = 7.3 Hz, 1H), 1.91 (t, J = 7.3 Hz, 2H), 1.45 (m, 2H), 1.41 – 1.30 (m, 2H), 1.27 – 1.14 (m, 2H). ^{13}C NMR (101 MHz, DMSO) δ 169.4, 143.4, 128.9, 128.0, 127.2, 75.6, 58.2, 53.3, 52.0, 32.6, 27.0, 26.4, 25.5. HRMS (ESI) calcd for C$_{23}$H$_{31}$N$_3$O$_2$ [M + H]$^+$ 382.2416, Found: 382.2488.

4.3.6. *7-(4-(diphenylmethyl)-piperazin-1-yl)-N-hydroxyheptanamide (7b)*. Pale yellow foamy powder (32.5 mg, 39% yield). ^{1}H NMR (400 MHz, DMSO) δ 10.27 (s, 1H), 8.60 (s, 1H), 7.40 (d, J = 7.8 Hz, 4H), 7.27 (t, J = 7.4 Hz, 4H), 7.16 (t, J = 7.0 Hz, 2H), 4.25 (s, 1H), 2.40 (s, 4H), 2.28 (s, 6H), 2.16 (t, J = 7.3 Hz, 1H), 1.90 (d, J = 7.2 Hz, 1H), 1.46 (d, J = 5.4 Hz, 2H), 1.37 (s, 2H), 1.23 (s, 4H).^{13}C NMR (101 MHz, DMSO) δ 169.5, 143.3, 128.9, 128.0, 127.2, 75.6, 58.1, 53.3, 51.8, 34.0, 32.6, 28.9, 27.0, 25.5. HRMS (ESI) calcd for C$_{24}$H$_{33}$N$_3$O$_2$ [M + H]$^+$ 396.2646, Found: 396.2645.

4.3.7.   *8-(4-(diphenylmethyl)-piperazin-1-yl)-N-hydroxyoctanamide (**8b**).* White foamy powder (159.8 mg, 56% yield).^{1}H NMR (400 MHz, DMSO) δ 10.31 (s, 1H), 7.41 (d, J = 7.5 Hz, 4H), 7.27 (t, J = 7.5 Hz, 4H), 7.17 (t, J = 7.2 Hz, 2H), 4.24 (s, 1H), 2.47 – 2.07 (m, 10H), 1.92 (t, J = 7.3 Hz, 2H), 1.51 – 1.41 (m, 2H), 1.37 (s, 2H), 1.22 (s, 6H). ^{13}C NMR (101 MHz, DMSO) δ 169.5, 143.3, 128.9, 128.0, 127.2, 75.6, 58.2, 53.3, 51.9, 32.7, 29.0, 28.9, 27.2, 26.6, 25.5. HRMS (ESI) calcd for $C_{25}H_{35}N_3O_2$ $[M + H]^+$ 410.2729, Found: 410.2803.

4.3.8.   *4-(4-(diphenylmethyl)-piperazin-1-ylmethyl)-N-hydroxy-benzamide (**9b**).* Pale yellow foamy powder (25.0 mg, 36% yield). ^{1}H NMR (400 MHz, DMSO) δ 11.14 (s, 1H), 8.97 (s, 1H), 7.87 (d, J = 8.1 Hz, 1H), 7.67 (d, J = 8.1 Hz, 1H), 7.39 (d, J = 7.4 Hz, 5H), 7.33 (d, J = 8.0 Hz, 1H), 7.26 (t, J = 7.5 Hz, 4H), 7.16 (t, J = 7.3 Hz, 2H), 4.26 (s, 1H), 3.51 (d, J = 12.2 Hz, 2H), 2.36 (d, J = 33.9 Hz, 8H). ^{13}C NMR (101 MHz, DMSO) δ 167.1, 142.8, 129.2, 128.7, 128.6, 128.4, 127.5, 126.7, 75.0, 61.4, 52.7, 52.6, 51.4. HRMS (ESI) calcd for $C_{25}H_{27}N_3O_2$ $[M + H]^+$ 402.2103, Found: 402.2165.

4.4.   Molecular docking

The synthesized inhibitors were sketched in ChemDraw software v. 7.0.1 and the ionization parameters (pH = 7.4) were calculated in MarvinSketch 6.1.0 (https://chemaxon.com/). The energy minimization of the synthesized ligands was performed in gas phase in Chem3D Ultra 7.0 software (Hartree-Fock 3-21G method by use of Gaussian 7.0.0). Optimized 3D structures of the inhibitors were used as deprotonated hydroxamates for molecular docking study. The crystal structure of the Histone Deacetylase 6 (PDB: 5EDU) was downloaded from PDB website (https://www.rcsb.org). Initial enzyme structure was protonated and tautomeric states of residues under physiological conditions were assigned using PDB2PQR 3.1.0 software accessed through server (https://server.poissonboltzmann.org/pdb2pqr). Catalytic water molecule in HDAC6 was retained for docking calculations. The structures of the inhibitors were treated flexible whereas the enzymes were kept rigid. Docking procedure was carried in metalloenzyme configuration mode in GOLD software v.5.8.1 with ChemScore calculated as scoring function. The validity of the docking procedures was examined by inspecting the RMSD value (RMSD <2Å) and docking poses were visualized in Discovery Studio software v.17.2.0.

4.5.   HDAC enzymes assay

Human recombinant C-ter-His-FLAG-HDAC1 (50051), HDAC-3/NcoR2 (50003), N-ter-GST-HDAC-6 (50006) and C-terminal His-tag-HDAC8 (50008) proteins were purchased from BPS Bioscience (San Diego, CA). Trichostatin A (Sigma-Aldrich) dissolved in DMSO was used as positive control, whereas DMSO was used as negative control. Synthesized compounds were dissolved in DMSO (v/v) and stored at −20 °C. Inhibition profiles for the synthesized compounds were monitored with bioluminogenic HDAC-Glo™ I/II assay (Promega Corp.)[37]. The compounds were tested at 8 different concentrations, with 2-fold dilution. Compound solutions were dispensed using the Echo 550® into 384 well assay plates (10 nL/well). This was followed by the addition of HDAC enzyme (5 µL/well) using the Multidrop liquid handling system and incubated for 10 min at room temperature. The final addition of the HDAC-Glo assay reagent (10 µL per well) was added to initiate the luciferase reaction. After 10 min incubation at room temperature, the luminescence was read on EnSpire Microplate Reader. All the experiments were performed in triplicate and the raw data obtained after screening was analyzed using Prism Software. The dose response curves were generated using a 4-parameter logistic fit in 8-point format yielding the IC_{50} values.

4.6.   Breast cancer cell cultures

Human breast adenocarcinoma cells (MCF-7, ATCC® HTB-22™) and triple negative breast cancer cells (MDA-MB-231, ATCC® HTB-26™) were obtained from the American Type Culture Collection (Rockville, MD). Cells were maintained as a monolayer culture in DMEM:Ham's 12 (1:1) medium (Sigma-Aldrich, St. Louis, MO, USA) supplemented with penicillin (192 U/mL), streptomycin (200 µg/mL) and 10% of heat-inactivated fetal calf serum (FCS). Cells were grown at 37 °C in 5% CO_2 and humidified air atmosphere, by twice weekly subculture.

4.6.1.   Cell viability (MTT) assay

Cytotoxic activity of synthesized 1-benzhydryl piperazine-based HDAC inhibitors was assessed on MDA-MB-231 and MCF-7 cells using MTT assay[61]. MDA-MB-231 (5×10^3 cells/well) and MCF-7 (5×10^3 cells/well) were treated with synthesized compounds in six different concentrations (100, 50, 25, 12.5, 6.25 and 3.13 µM), each concentration is added in five replicates. MTT solution (3-(4, 5-dimethylthiazol-2-yl)-2,5-dyphenyl tetrazolium bromide) (Sigma-Aldrich, St. Louis, USA) was added to each well (20 µL) after 48 hours. After 4 hours of incubation, 100 µL of 10% SDS was added in each well and incubated at 37 °C. On the next day, the absorbance at 570 nm was recorded. The ratio in absorbance (570 nm) values between treated and control cells

multiplied by 100 was used to calculate cell survival (%). The concentration of synthesized HDAC inhibitors that reduce cell viability by 50% is defined as IC_{50} value and compared to the vehicle control.

4.6.2. Apoptosis assay

Examined breast cancer cells (MDA-MB-231 and MCF-7) were stained with annexin V–fluorescein isothiocyanate/and 7AAD (BD Pharmingen, San Diego, CA, USA) and the samples were prepared following the specifications given by manufacturer. The population of apoptotic cells was analyzed by flow cytometry using a FACS-Calibur cytometer using Cell Quest computer software (Becton Dickinson, Heidelberg, Germany).

4.6.3. Cell cycle analysis

MDA-MB-231 and MCF-7 cells were treated with tested compounds for specified time course. After treatment, examined cells were washed in cold PBS and incubated for 30 min in 96% ethanol on ice, centrifuged and incubated with 80 μL RNase A (200μg/mL/mL) and 50 μL propidium iodide (50 μg/mL) for 30 min at 37 °C. The cell cycle was analyzed by FACS Calibur E440 (Becton Dickinson) flow cytometer and Cell Quest software. Results were presented as a percentage of cell cycle phases.

4.6.4. Detection of mitochondrial membrane potential

Mitochondria membrane potential was determined by the fluorescent dye JC-1[62]. After treatment with different concentrations of compounds under standard culture conditions for 48 h, the cells were stained with 40 μL of JC-1 (final concentration 15.4μM) and incubated under standard conditions for 15 min. The fluorescence intensity of cells was determined by flow cytometry.

4.6.5. Measurement of total intracellular reactive oxygen species

Generation of reactive oxygen species (ROS) was measured using a 20,70-dichlorodihydrofluorescein diacetate (DCFH-DA). Briefly, MDA-MB-231 cells were treated with investigated copounds and the untreated cells were maintained as the control. After incubation period of 24 or 48 h, the cells were harvested, washed twice, resuspended in 10mM DCFH-DA and incubated at 37 °C for 30 min in the dark. The levels of intracellular
ROS were examined with flow cytometry (FACS Calibur, BD Biosciences, USA). Data acquisition and analyses were carried out using Cell Quest software (BD Biosciences, USA).

4.6.6. Generation and analysis of tumor spheroids

MDA-MB-231 cells were seeded at cell density of 1000 c/w in 100 μL of DMEM containing 10% FCS in a low attachment NunclonSphera 96-well ultra-low attachment plate (Thermo Scientific Nunc™) to form multicellular tumor spheroids for 4days. The formation and growth of tumor spheroids were examined and imaged with a XXX microscope, using 10x objective. MDA-MB-231 tumor spheroids were treated by carefully adding 50 μL of the medium with fresh nutrient medium for control spheres or with **compound**-supplemented medium (50μM) for treated spheres for another 72 h. The cytotoxicity of **compounds** toward the MDA-MB-231 tumor spheroids was investigated by MTT assay

In a anther series experiments MDA-MB-231 cells were seeded in co-culture with investigated compounds (IC_{50} and 50μM) at cell density of 2000 c/w in 150 μL of DMEM containing 10% FCS in a low attachment NunclonSphera 96-well ultra-low attachment plate (Thermo Scientific Nunc™) to form multicellular tumor spheroids for 4 days. The formation and growth of tumor spheroids were examined and imaged with a XXX microscope, using 4x objective. The cytotoxicity of **compounds** toward the MDA-MB-231 tumor spheroids was investigated by MTT assay

4.6.5. Bicameral motility and invasion assay

To determine MDA-MB-231 cell migration and invasion cell capacities Corning® Costar® Transwell® cell culture inserts with 8.0 μm pore polycarbonate filters (Sigma Aldrich, CLS3464) and Corning™ BioCoat™ Matrigel™ Invasion Chamber with Corning Matrigel Matrix™ cell culture inserts (Thermo fisher scientific) respectively were used . Briefly, 6×10^4 cells in 200 μL were seeded in the upper chamber and the bottom chamber was filled with 800 μL of medium. After 24 h under indicated treatments, the remaining cells in the upper chamber were gently removed with a cotton swab moistened with medium and insert were carefully washed 2× with 37°C warmed PBS. Then, attached cells at the bottom side of membrane were fixed by immersing in ice cold methanol for two min and stained with 0.1% crystal violet for 15 min at room temperature. Stained cells were photographed and quantified using NIH-Image J software.

4.6.6. Wound-Healing Assay

To determine MCF-7 cells migration properties, 1×10^5 cells were seeded in 24 well plates and cultured until confluent. Then, cell monolayers scratch were made using a sterile pipette 200 μL tip, and cell cultures were

allowed to grow for 24 h under indicated treatments. At the final of incubation period, culture medium was removed and wells were washed 2× with PBS, then cells were two min fixed with ice-cold methanol and 15 min stained with 0.1% crystal violet. In addition, cell monolayers were fixed and stained just after scratch was made as zero time migration. Finally, cell migration into the scratch area was documented by inverted light microscopy and quantified using NIH-Image J software[63].

4.7. Animal study in the zebrafish (*Danio rerio*) model
Embryos of wild type (AB) and transgenic *Tg*(*fli1*:EGFP)i114 and *Tg*(*-2.8fabp10a*:EGFP) zebrafish (*Danio rerio*) lines were kindly provided by Dr. Ana Cvejić (Wellcome Trust Sanger Institute, Cambridge, UK) and raised to adult stage in a temperature- and light-controlled zebrafish facility at 28 °C and standard 14-10 h light-dark photoperiod. Adult fish were regularly fed with commercially dry food (SDS300 granular food; Special Diet Services, Essex; UK and TetraMinTM flakes; Tetra Melle, Germany) twice per day and *Artemia nauplii* daily. All experiments involving zebrafish were performed in compliance with the European directive 2010/63/EU and the ethical guidelines of the Guide for Care and Use of Laboratory Animals of the Institute of Molecular Genetics and Genetic Engineering, University of Belgrade.

4.7.1. Acute and developmental toxicity assessment
Toxicity evaluation of the tested compounds in the zebrafish model was carried out following the general rules of the OECD Guidelines for the Testing of Chemicals (OECD, 2013, Test No. 236)[64] and procedures described in the literature.[65] Briefly, wild type (AB) zebrafish produced by pair-wise mating were collected, washed of debris and distributed into 24 well plates containing 10 embryos/well and 1 mL of E3 medium (5 mM NaCl, 0.17 mM KCl, 0.33 mM CaCl$_2$ and 0.33 mM MgSO$_4$×7H$_2$O in distilled water), and raised at 28 °C.
To assess acute (lethality), inner organ and developmental (teratogenicity) toxicity, the embryos at 6 h post fertilization (hpf) stage were treated with six different concentrations of each tested compound (100, 50, 25, 12.5, 6.25 and 3.13 μM). Stock solutions of test substances were made in DMSO. Embryo water and DMSO (0.25%) were used as negative and positive controls, respectively. Experiment was performed three times using 20 embryos per concentration. Treated embryos were inspected for 22 toxicological parameters (Table S2) every day by 120 hpf upon an steremicroscope (Carl Zeiss™ Stemi 508 doc Stereomicroscope, Germany). Dead embryos were discarded every 24 h. At 120 hpf, embryos have been anesthetized by addition of 0.1% (w/v) tricaine solution (Sigma-Aldrich, St. Louis, MO), photographed and killed by freezing at −20 °C for ≥ 24 h.

4.7.2. Anti-angiogenic activity assessment
The inhibitory activity of **8b** on angiogenesis was examined using embryos of transgenic zebrafish *Tg*(*fli1*:EGFP) line with GFP-labelled endothelial cells, as previously described[65]. Briefly, embryos at 6-8 hpf stage were exposed to three non-toxic concentrations and incubated at 28 °C by 48 hpf. At 48 hpf, the treated embryos were anesthetized with 0.02% tricaine, imaged under a fluorescence microscope (Olympus BX51, Applied Imaging Corp., San Jose, CA, USA) and analyzed for the development of intersegmental blood vessels (ISVs). The experiment was performed three times using 10 embryos per concentration. ISV vessels lengths were measured using ImageJ program, and expressed as mean value with standard deviation. Inhibitory effect of the applied treatment was determined in relation to the control (DMSO-treated) group, arbitrarily set to 100%.

4.7.3. Anti-cancer activity evaluation in human zebrafish cell derived (CDX) xenografts
Cell-lines culture preparation
The human breast carcinoma MDA-MB 231 cell-line was cultured in DMEM:Ham's 12 (1:1) medium (Sigma-Aldrich, St. Louis, MO, USA) supplemented with 10% FBS (Sigma- Aldrich, St. Louis, MO, USA), 100 μg/mL streptomycin and 100 U/mL penicillin (Sigma- Aldrich, St. Louis, MO, USA), and grown as a monolayer in humidified atmosphere of 95% air and 5% CO$_2$ at 37 °C. Prior to microinjection, the cells were washed once with PBS and trypsinized (0.25% trypsin/0.53 mM EDTA) (Sigma- Aldrich, St. Louis, MO, USA) to obtain a single cell suspension. After centrifugation at 1200 rpm for 5 min, the cells were resuspended in serum-free DMEM medium and labelled with 2 μM Cell Tracker TM Red CMTPX (ThermoFisher Scientific) according to the manufacturer's instructions.

4.7.4. Zebrafish xenografts and treatment efficacy assessment
The zebrafish xenografts with human MDA-MB-231 cells were established according to the previously described procedure with slight modification[66]. A day before the microinjections, *Tg*(*fli1*:EGFP) embryos kept at 28 °C were manually dechorionated. At 48 hpf stage, 5 nL of MDA-MB 231 cells suspension containing 150 labelled cells was microinjected into the yolk of anesthetized embryos by a pneumatic picopump (PV820, World Precision Instruments, USA). Exact number of cells was confirmed by dispensing the injected volume onto a microscope slide and by visual counting. After injection, embryos were incubated to recover for at least for 60 min at 28 °C, dead embryos were removed, while alive embryos were transferred into 24-well plates containing

1 mL of E3 water and 10 embryos per well. The injected xenografts were treated with the three doses of **8b** (3.13, 6.25 and 12.5 μM), and maintained at 31-32 °C by 120 hpf. DMSO (0.25%) was used as a negative control. The survival and development of the xenografted embryos was recorded every day until the end of experiment (3 days post injection = 3 dpi), when anesthetized xenografts were processed by fluorescent microscopy. The tumor size, number of xenografts with disseminated tumor cells in the caudal region, and number of disseminated cells per embryo have been determined. The tumor size was determined by the fluorescent images using ImageJ programme. The experiment was repeated two times using 10 embryos per concentration.

4.8. Statistical analysis

The experimental results were expressed as mean values ± SD. The χ^2 test was used to determine the differences in anti-angiogenic phenotypes between the untreated and treated groups. In other experiments, the differences between the untreated and treated groups were evaluated using the one-way ANOVA followed by a comparison of the means by Bonferroni test (P = 0.05). SPSS 20 software package (SPSS Inc., Chicago, IL) was used to analyze experimental data, whereas graphical representation of the results was prepared in GraphPad Prism 6 (GraphPad Software, Inc., San Diego, California, USA).

Declaration of competing interest

The authors declare that they have no known competing financial interests or personal relationships that could have appeared to influence the work reported in this paper.

Acknowledgements

Appendix A. Supplementary data

References

[1] A. C. Wolff, M. E. H. Hammond, D. G. Hicks, M. Dowsett, L. M. McShane, K. H. Allison, D. C. Allred, J. M. S. Bartlett, M. Bilous, P. Fitzgibbons, W. Hanna, R. B. Jenkins, P. B. Mangu, S. Paik, E. A. Perez, M. F. Press, P. A. Spears, G. H. Vance, G. Viale, D. F. Hayes, American Society of Clinical Oncology, College of American Pathologists, *J. Clin. Oncol. Off. J. Am. Soc. Clin. Oncol.* **2013**, *31*, 3997–4013.

[2] A. Kadamkulam Syriac, N. S. Nandu, J. P. Leone, *Breast Cancer Targets Ther.* **2022**, *14*, 1–13.

[3] M. Cobleigh, D. A. Yardley, A. M. Brufsky, H. S. Rugo, S. M. Swain, P. A. Kaufman, D. Tripathy, S. A. Hurvitz, J. O'Shaughnessy, G. Mason, V. Antao, H. Li, L. Chu, M. Jahanzeb, *Clin. Cancer Res. Off. J. Am. Assoc. Cancer Res.* **2020**, *26*, 1105–1113.

[4] G. Bianchini, C. De Angelis, L. Licata, L. Gianni, *Nat. Rev. Clin. Oncol.* **2022**, *19*, 91–113.

[5] K. P. Nephew, T. H.-M. Huang, *Cancer Lett.* **2003**, *190*, 125–133.

[6] J. E. Lee, M.-Y. Kim, *Semin. Cancer Biol.* **2021**, DOI 10.1016/j.semcancer.2021.03.025.

[7] F. Dang, W. Wei, *Semin. Cancer Biol.* **2021**, DOI 10.1016/j.semcancer.2021.03.001.

[8] T. R. Singh, S. Shankar, R. K. Srivastava, *Oncogene* **2005**, *24*, 4609–4623.

[9] B. G. Debeb, L. Lacerda, W. Xu, R. Larson, T. Solley, R. Atkinson, E. P. Sulman, N. T. Ueno, S. Krishnamurthy, J. M. Reuben, T. A. Buchholz, W. A. Woodward, *STEM CELLS* **2012**, *30*, 2366–2377.

[10] A. K. Knutson, J. Welsh, T. Taylor, S. Roy, W.-L. W. Wang, M. Tenniswood, *Oncol. Rep.* **2012**, *27*, 849–853.

[11] Y. Chen, Y.-H. Tsai, S.-H. Tseng, *Int. J. Mol. Sci.* **2017**, *18*, 258.

[12] W.-J. Huang, Y.-A. Tang, M.-Y. Chen, Y.-J. Wang, F.-H. Hu, T.-W. Wang, S.-W. Chao, H.-W. Chiu, Y.-L. Yeh, H.-Y. Chang, H.-F. Juan, P. Lin, Y.-C. Wang, *Cancer Lett.* **2014**, *346*, 84–93.

[13] X. Bian, Z. Liang, A. Feng, E. Salgado, H. Shim, *Biochem. Pharmacol.* **2018**, *147*, 30–37.

[14] M. S. Kim, H. J. Kwon, Y. M. Lee, J. H. Baek, J.-E. Jang, S.-W. Lee, E.-J. Moon, H.-S. Kim, S.-K. Lee, H. Y. Chung, C. W. Kim, K.-W. Kim, *Nat. Med.* **2001**, *7*, 437–443.

[15] J. Roche, P. Bertrand, *Eur. J. Med. Chem.* **2016**, *121*, 451–483.

[16] "Structures of a histone deacetylase homologue bound to the TSA and SAHA inhibitors | Nature," can be found under https://www.nature.com/articles/43710, **n.d.**

[17] T. C. S. Ho, A. H. Y. Chan, A. Ganesan, *J. Med. Chem.* **2020**, *63*, 12460–12484.

[18] A. Valenzuela-Fernández, J. R. Cabrero, J. M. Serrador, F. Sánchez-Madrid, *Trends Cell Biol.* **2008**, *18*, 291–297.

[19] G. I. Aldana-Masangkay, K. M. Sakamoto, *J. Biomed. Biotechnol.* **2010**, *2011*, e875824.

[20] M. Rey, M. Irondelle, F. Waharte, F. Lizarraga, P. Chavrier, *Eur. J. Cell Biol.* **2011**, *90*, 128–135.

[21] D. Arsenault, K. Brochu-Gaudreau, M. Charbonneau, C. M. Dubois, *PLOS ONE* **2013**, *8*, e55529.

[22] C. Hubbert, A. Guardiola, R. Shao, Y. Kawaguchi, A. Ito, A. Nixon, M. Yoshida, X.-F. Wang, T.-P. Yao, *Nature* **2002**, *417*, 455–458.

[23] D. Kaluza, J. Kroll, S. Gesierich, T.-P. Yao, R. A. Boon, E. Hergenreider, M. Tjwa, L. Rössig, E. Seto, H. G. Augustin, A. M. Zeiher, S. Dimmeler, C. Urbich, *EMBO J.* **2011**, *30*, 4142–4156.

[24] Y. Hai, D. W. Christianson, *Nat. Chem. Biol.* **2016**, *12*, 741–747.
[25] Y. Miyake, J. J. Keusch, L. Wang, M. Saito, D. Hess, X. Wang, B. J. Melancon, P. Helquist, H. Gut, P. Matthias, *Nat. Chem. Biol.* **2016**, *12*, 748–754.
[26] Y. Sixto-López, J. A. Gómez-Vidal, N. de Pedro, M. Bello, M. C. Rosales-Hernández, J. Correa-Basurto, *Sci. Rep.* **2020**, *10*, 10462.
[27] Y.-L. Hsieh, H.-J. Tu, S.-L. Pan, J.-P. Liou, C.-R. Yang, *Biochim. Biophys. Acta BBA - Mol. Cell Res.* **2019**, *1866*, 992–1003.
[28] H. Song, X. Niu, J. Quan, Y. Li, L. Yuan, J. Wang, C. Ma, E. Ma, *Bioorganic Chem.* **2020**, *97*, 103679.
[29] Y. Li, J. Quan, H. Song, D. Li, E. Ma, Y. Wang, C. Ma, *Bioorganic Chem.* **2021**, *114*, 105081.
[30] Y. Depetter, S. Geurs, R. D. Vreese, S. Goethals, E. Vandoorn, A. Laevens, J. Steenbrugge, E. Meyer, P. de Tullio, M. Bracke, M. D'hooghe, O. D. Wever, *Int. J. Cancer* **2019**, *145*, 735–747.
[31] M. K. Ediriweera, K. H. Tennekoon, S. R. Samarakoon, *Drug Discov. Today* **2019**, *24*, 685–702.
[32] D. Ruzic, M. Petkovic, D. Agbaba, A. Ganesan, K. Nikolic, *Mol. Inform.* **2019**, *38*, 1800083.
[33] "Molecular descriptors calculation - Dragon - Talete srl," can be found under http://www.talete.mi.it/products/dragon_description.htm, **n.d.**
[34] K. Krukowski, J. Ma, O. Golonzhka, G. O. Laumet, T. Gutti, J. H. van Duzer, R. Mazitschek, M. B. Jarpe, C. J. Heijnen, A. Kavelaars, *Pain* **2017**, *158*, 1126–1137.
[35] K. V. Butler, J. Kalin, C. Brochier, G. Vistoli, B. Langley, A. P. Kozikowski, *J. Am. Chem. Soc.* **2010**, *132*, 10842–10846.
[36] L. Santo, T. Hideshima, A. L. Kung, J.-C. Tseng, D. Tamang, M. Yang, M. Jarpe, J. H. van Duzer, R. Mazitschek, W. C. Ogier, D. Cirstea, S. Rodig, H. Eda, T. Scullen, M. Canavese, J. Bradner, K. C. Anderson, S. S. Jones, N. Raje, *Blood* **2012**, *119*, 2579–2589.
[37] F. Halley, J. Reinshagen, B. Ellinger, M. Wolf, A. L. Niles, N. J. Evans, T. A. Kirkland, J. M. Wagner, M. Jung, P. Gribbon, S. Gul, *J. Biomol. Screen.* **2011**, *16*, 1227–1235.
[38] N. J. Porter, F. F. Wagner, D. W. Christianson, *Biochemistry* **2018**, *57*, 3916–3924.
[39] N. J. Porter, A. Mahendran, R. Breslow, D. W. Christianson, *Proc. Natl. Acad. Sci.* **2017**, *114*, 13459–13464.
[40] J. D. Osko, N. J. Porter, P. A. Narayana Reddy, Y.-C. Xiao, J. Rokka, M. Jung, J. M. Hooker, J. M. Salvino, D. W. Christianson, *J. Med. Chem.* **2020**, *63*, 295–308.
[41] I. N. Gaisina, W. Tueckmantel, A. Ugolkov, S. Shen, J. Hoffen, O. Dubrovskyi, A. Mazar, R. A. Schoon, D. Billadeau, A. P. Kozikowski, *ChemMedChem* **2016**, *11*, 81–92.
[42] I. M. Ghobrial, T. E. Witzig, A. A. Adjei, *CA. Cancer J. Clin.* **2005**, *55*, 178–194.
[43] R. Jan, G.-S. Chaudhry, *Adv. Pharm. Bull.* **2019**, *9*, 205–218.
[44] B. Perillo, M. Di Donato, A. Pezone, E. Di Zazzo, P. Giovannelli, G. Galasso, G. Castoria, A. Migliaccio, *Exp. Mol. Med.* **2020**, *52*, 192–203.
[45] S. A. Langhans, *Front. Pharmacol.* **2018**, *9*.
[46] C. R. Justus, N. Leffler, M. Ruiz-Echevarria, L. V. Yang, *J. Vis. Exp. JoVE* **2014**, 51046.
[47] K. Wolf, S. Alexander, V. Schacht, L. M. Coussens, U. H. von Andrian, J. van Rheenen, E. Deryugina, P. Friedl, *Semin. Cell Dev. Biol.* **2009**, *20*, 931–941.
[48] T. Q. Pham, K. Robinson, L. Xu, M. N. Pavlova, S. X. Skapek, E. Y. Chen, *Oncogene* **2021**, *40*, 578–591.
[49] S. Saji, M. Kawakami, S. Hayashi, N. Yoshida, M. Hirose, S. Horiguchi, A. Itoh, N. Funata, S. L. Schreiber, M. Yoshida, M. Toi, *Oncogene* **2005**, *24*, 4531–4539.
[50] K. Azuma, T. Urano, K. Horie-Inoue, S. Hayashi, R. Sakai, Y. Ouchi, S. Inoue, *Cancer Res.* **2009**, *69*, 2935–2940.
[51] C. A. MacRae, R. T. Peterson, *Nat. Rev. Drug Discov.* **2015**, *14*, 721–731.
[52] C. Chakraborty, C. H. Hsu, Z. H. Wen, C. S. Lin, G. Agoramoorthy, *Curr. Drug Metab.* **n.d.**, *10*, 116–124.
[53] S. Cassar, I. Adatto, J. L. Freeman, J. T. Gamse, I. Iturria, C. Lawrence, A. Muriana, R. T. Peterson, S. Van Cruchten, L. I. Zon, *Chem. Res. Toxicol.* **2020**, *33*, 95–118.
[54] H.-C. Lee, C.-Y. Lin, H.-J. Tsai, *Pharmaceuticals* **2021**, *14*, 500.
[55] M. Cully, *Nat. Rev. Drug Discov.* **2019**, *18*, 811–813.
[56] J. Folkman, *Nat. Med.* **1995**, *1*, 27–30.
[57] N. Ferrara, R. S. Kerbel, *Nature* **2005**, *438*, 967–974.
[58] A. Albini, G. Pennesi, F. Donatelli, R. Cammarota, S. De Flora, D. M. Noonan, *J. Natl. Cancer Inst.* **2010**, *102*, 14–25.
[59] R. Fior, V. Póvoa, R. V. Mendes, T. Carvalho, A. Gomes, N. Figueiredo, M. G. Ferreira, *Proc. Natl. Acad. Sci. U. S. A.* **2017**, *114*, E8234–E8243.
[60] R. White, K. Rose, L. Zon, *Nat. Rev. Cancer* **2013**, *13*, 624–636.
[61] T. Mosmann, *J. Immunol. Methods* **1983**, *65*, 55–63.
[62] M. Reers, S. T. Smiley, C. Mottola-Hartshorn, A. Chen, M. Lin, L. B. Chen, in *Methods Enzymol.*, Academic Press, **1995**, pp. 406–417.
[63] D. Trivanović, A. Jauković, J. Krstić, S. Nikolić, I. Okić Djordjević, T. Kukolj, H. Obradović, S. Mojsilović, V. Ilić, J. F. Santibanez, D. Bugarski, *IUBMB Life* **2016**, *68*, 190–200.
[64] OECD, **2013**.
[65] J. Delasoie, A. Pavic, N. Voutier, S. Vojnovic, A. Crochet, J. Nikodinovic-Runic, F. Zobi, *Eur. J. Med. Chem.* **2020**, *204*, 112583.
[66] C. Tulotta, C. Stefanescu, E. Beletkaia, J. Bussmann, K. Tarbashevich, T. Schmidt, B. E. Snaar-Jagalska, *Dis. Model. Mech.* **2016**, *9*, 141–153.